National Institute of Standards and Technology
Technology Administration, U.S. Department of Commerce

NIST Technical Note 1527

Numerical Comparison of Currents Induced on an Object in Free-Space and in a TEM Cell

Per E. Fornberg
Christopher L. Holloway
Perry F. Wilson

NIST Technical Note 1527

Numerical Comparison of Currents Induced on an Object in Free-Space and in a TEM Cell

Per E. Fornberg
Christopher L. Holloway
Perry F. Wilson

Electromagnetics Division
National Institute of Standards and Technology
325 Broadway
Boulder, CO 80305

July 2006

U.S. Department of Commerce
Carlos M. Gutierrez, Secretary

Technology Administration
Robert Cresanti, Under Secretary of Commerce for Technology

National Institute of Standards and Technology
William Jeffrey, Director

National Institute of Standards and Technology Technical Note 1527
Natl. Inst. Stand. Technol. Tech. Note 1527, 50 pages (July 2006)
CODEN: NTNOEF

U.S. Government Printing Office
Washington: 2005

For sale by the Superintendent of Documents, U.S. Government Printing Office
Internet bookstore: gpo.gov Phone: 202-512-1800 Fax: 202-512-2250
Mail: Stop SSOP, Washington, DC 20402-0001

Contents

Numerical Comparison of Currents Induced on an Object in Free-Space and in a TEM Cell

Per E. Fornberg, Christopher L. Holloway, and Perry F. Wilson

Electromagnetics Division
National Institute of Standards and Technology
325 Broadway, Boulder, CO 80305

The finite-difference time-domain (FDTD) method is used to investigate whether the currents induced on equipment under test (EUT) in a transverse electromagnetic (TEM) cell are similar to those induced in a free-space environment. The approach is to simulate an identical EUT in both environments and determine a correlation based on the respective current distributions. The effect of the ratio of EUT to TEM cell size on the correlation to free space is also investigated.

Key words: finite-difference time-domain, transverse electromagnetic cell

1. Motivation and Introduction

An immunity test of an EUT involves exposing the UET to a known incident field and determining if its operation is affected. In most cases the desired incident field is an ideal plane wave. An ideal plane is a mathematical construct and cannot be physically realized. Thus, actual susceptibility testing is done using approximations to a plane wave. One approach to generating an approximate plane wave is to excite the TEM mode on a transmission line. Enclosed transmissions lines, or TEM cells are commonly used as test fixtures for this purpose.

This investigation examines how well a TEM cell approximates an ideal plane wave susceptibility test. In particular numerical simulations are used to model the currents induced on a representative EUT in both free space and in a TEM cell. Various correlation metrics are then used to compare the induced currents on the EUT.

1.1 The Transverse Electromagnetic (TEM) Cell

The transverse electromagnetic cell, sometimes referred to as a “Crawford Cell” after Myron L. Crawford of NIST, was investigated as an EMC test facility beginning in the 1970’s. The TEM cell, shown in Figures 1(a and b), consists of a section of rectangular coaxial transmission line, tapered at each end to adapt to standard coaxial connectors. The TEM cell offers a shielded environment and a known field distribution based upon the fundamental TEM mode [4]. These cells are often used for probe calibration, due to the standard fields they generate. The TEM cell has also found use for EMC radiated and susceptibility measurements at frequencies below 1 GHz. Since the fundamental TEM field distribution inside the chamber is similar to that of a plane wave, the environment is like that of a fully anechoic chamber.

The use of TEM cells for immunity testing offers several advantages over the use of an anechoic chamber. One advantage is the elimination of ambient fields without the introduction of measurement problems associated with shielded or anechoic chambers. In addition, uniform and readily determined fields are generated inside. A primary limitation of the TEM cell is the reduced test volume (size of EUT), since a center conductor (septum) is required. Their use is therefore primarily limited to the testing of smaller portable devices, such as laptop computers or cell phones. Another limitation of the TEM cell is the excitation of higher-order modes and their associated resonances that perturb the TEM mode field distribution [5]. Reducing the size of the cell increases the frequency range before higher-order modes appear, but this further decreases the test volume within the chamber. To limit the excitation of higher-order modes, and to ensure that incident fields are a uniform plane wave, common practice indicates the EUT should be no larger than one-third the separation distance between the septum (inner conductor) and corresponding cell wall (outer conductor) [6].

(a) (b)

Figure 1: Picture of a TEM cell with a portion of the sidewall removed to reveal the septum (a) and larger room-sized TEM cell (b).

1.2 The Broadband Transverse Electromagnetic “GTEM” Cell

The “GTEM” cell is a modification of the TEM cell that increases its bandwidth and test volume. A “GTEM” cell is essentially a tapered section of a rectangular coaxial transmission line that is terminated by a matched load. The septum is vertically offset (positioned off center) to increase the test volume. As with the TEM cell, the principle behind a “GTEM” cell is to utilize the fundamental TEM mode, which propagates in a coaxial transmission line. The RF absorber placed on the terminating wall helps to dampen the higher-order modes, greatly extending the usable frequency range up to several gigahertz. As a result of these modifications, the “GTEM” cell represents a viable alternative to OATS or anechoic chambers for facilitating EMC emissions and susceptibility testing.

Figure 2(a and b) displays the outside and inside of a “GTEM” chamber. A coaxial feed is connected to an adapter at the far (small) end of the chamber shown in Figure 2(a). A photograph taken inside the chamber and facing the absorber is shown in Figure 2(b), where the vertically offset center conductor (septum) is seen suspended from the top wall at the top of the picture. When an EUT is inserted into the chamber, it is placed between the lower wall and septum, shown in Figure 2(b).

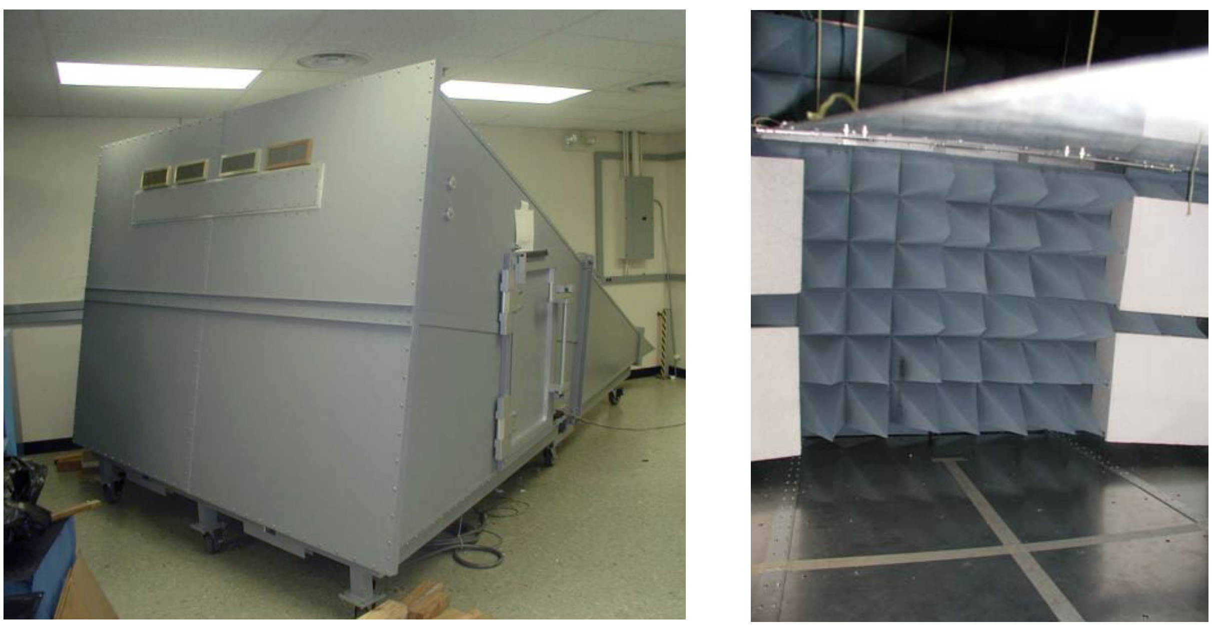

(a) (b)

Figure 2: Photographs of (a) the outside of a “GTEM” cell and (b) the inside absorber on the terminal wall.

Some research has been concerned with correlating "GTEM" to OATS measurements, and numerous publications have addressed this issue [7-9]. The generally good correlation obtained between these measurements has increased the interest in utilizing "GTEM" cells as alternatives to an OATS or anechoic chambers. This interest caused the FCC to release a Public Notice in 1993 stating they would accept "GTEM" measurement data under "limited conditions" [10].

1.3 "Modernizing" Current Emission and Immunity Standards

There is growing support within the EMC community to update the emission and susceptibility standards so that products are tested in a more realistic environment [11]. Since the OATS emission standard was adopted by the FCC in 1979, the proliferation of faster and smaller devices has dramatically changed the electromagnetic environment from that of 20 years ago. The OATS standard is based on studies, conducted in the 1960's, that were concerned with reducing interference to television antennas from office machines [12]. Today, few people receive television programs from transmitter broadcasts, but the number of products utilizing the electromagnetic spectrum (intentionally or not) has greatly increased. This trend will only increase in the near future with emerging technologies such as high-speed wireless networks.

In an attempt to "modernize" the regulatory standard, and to allow for lower cost facilities, alternative test procedures are being considered. Two such alternatives for emissions and susceptibility testing are the "GTEM" cell, discussed above, and the reverberation chamber. The reverberation chamber will not be discussed in this report, but the interested reader is referred to descriptions in the literature [13-16].

Before any standards can be rewritten, that would allow for use of "GTEM" cells as an alternative in certification testing for frequencies from a few megahertz to several gigahertz, its performance must be carefully examined. The research presented here numerically investigates the effectiveness of a "GTEM" cell for immunity testing. This work furthers the investigation by examining the correlation between the currents induced on an EUT of various sizes in both a free-space and a modified TEM cell geometry. The TEM cell geometry investigated is similar to that of a "GTEM" cell, with the exception that the cross-sectional area of the cell is maintained. This is similar to the center section of a TEM cell and differs from a "GTEM" cell, where the entire length of the cell is tapered. However, the model is similar to that of a "GTEM" cell in that an absorbing boundary is present to reduce the higher-order modes (see fig. 3b). This modified TEM cell geometry represents a parallel-plate waveguide. The simulation models will be explained in further detail later in the report.

2. Numerical Approach

A numerical approach was adopted for this research because it offers a few important benefits over measurements. Foremost, it allows for the probing of any field or current value without influencing the simulation. The currents on the EUT can be examined and compared, something that cannot be measured in practice. In addition, a numerical approach permits quick and easy alterations of the simulation model. This allows for the simulation of numerous relative EUT sizes within the TEM cell. Performing measurements alone would require multiple EUT's (or TEM cells) of various sizes. Finally, the simulations are closer to ideal, partly because the simulations are lossless and measurement errors are eliminated, which aids in the examination of results.

The EUT in the simulation models was a square metal box with an aperture on the front surface facing the incident plane wave. To examine the currents induced on the box (EUT) and localized field levels, electric and magnetic fields probes were positioned both inside and outside the box. The tangential magnetic field components along the outside surfaces of the box were stored at each time step for use in determining the induced currents. In addition, various point probes were placed at certain locations near the aperture and scattered inside the box to monitor the dominant z-component of the electric field. These probes provided both qualitative evidence that the model is simulating as intended and quantitative data of the field distribution surrounding the box. The data gathered from these probes were used to compare the electrical stresses imposed on the EUT between the TEM cell (parallel-plate waveguide) and free-space models.

The two simulation models are illustrated in Figure 3. The free-space (fully anechoic) environment (Figure 3(a)) was replicated by surrounding the metal box with a region of air and truncating the computational volume with an absorbing boundary condition. This boundary absorbs all incident energy, essentially producing an infinite free-space environment. The TEM cell model (Figure 3(b)) was created by replicating the environment shown within the shaded area of Figure 4, which depicts the cross section of a TEM cell. Perfect electrically conducting metal walls were positioned along the upper and lower sides of the simulation model to simulate the upper (or lower) wall and septum (center plate) present in a TEM cell. The absorbing boundary remained present along the adjacent four sides. Within the shaded area of Figure 4, there exists approximate field uniformity of the TEM mode. Since field uniformity is assumed, only two metal walls, representing the septum and lower side of the TEM wall, were included in the model. If the sides perpendicular to the septum were included, the entire TEM cell geometry would have to be modeled, greatly increasing the model's size.

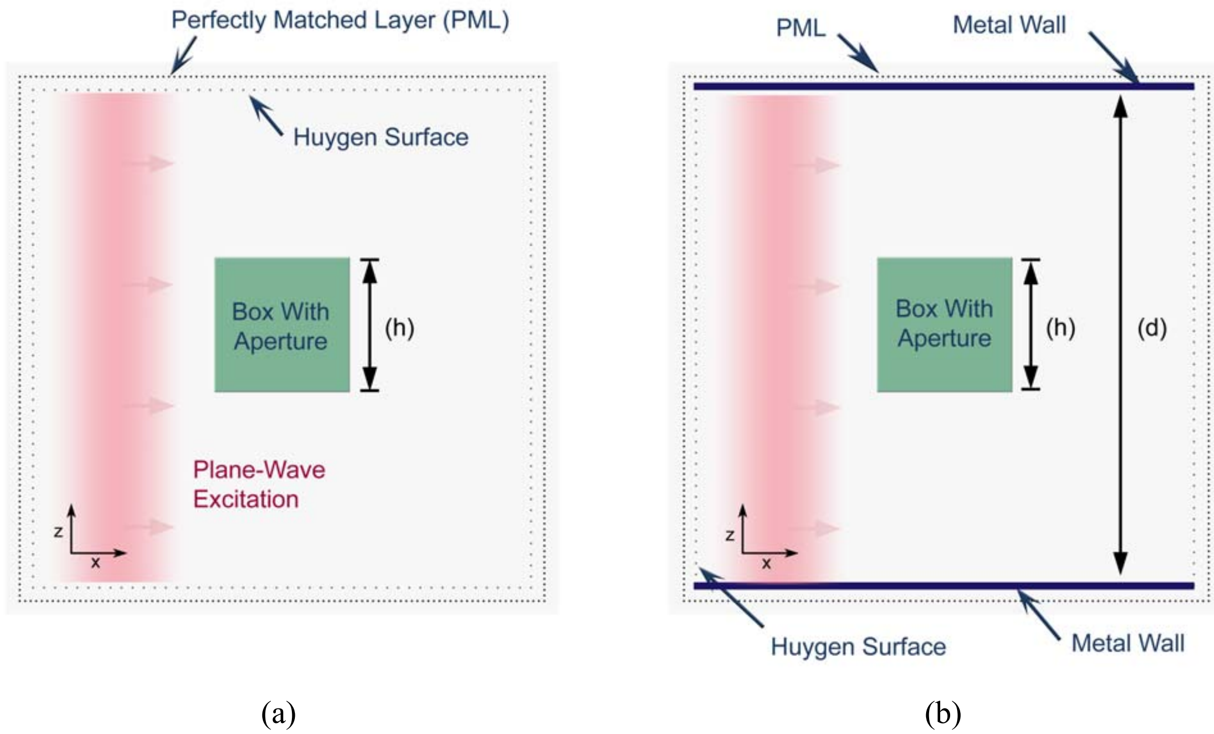

Figure 3: Free-space (a) and TEM cell (b) simulation models.

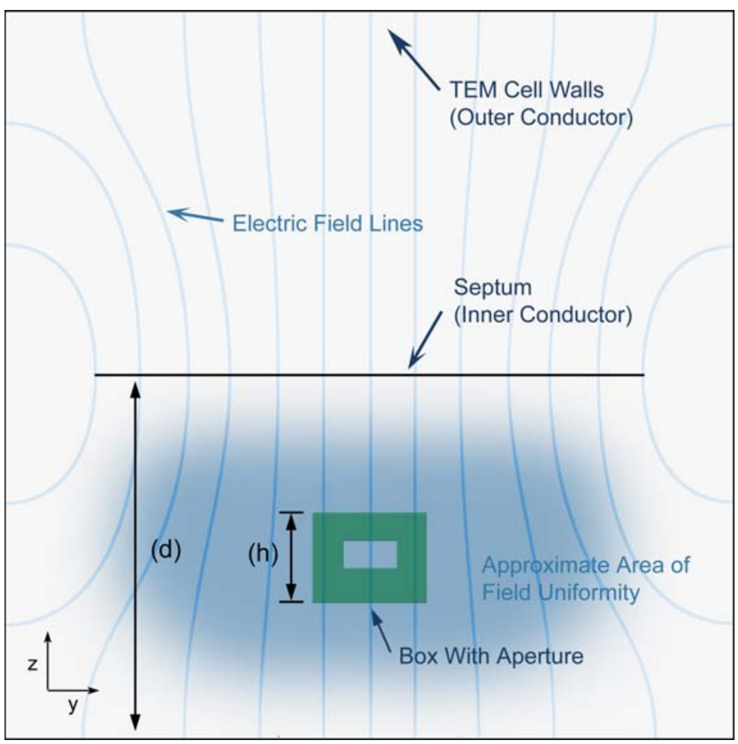

Figure 4: Cross section of a typical TEM cell.

To investigate the effect of relative EUT size (*h/d* ratio) in a TEM cell, either the dimensions of the EUT or the volume of the TEM cell chamber can be varied. For programming simplicity, the height (*h*) of the EUT was held constant while the separation (*d*) between the metal walls in the TEM cell model was varied; this corresponds to the separation between the lower outer wall and the septum. In all simulations, the EUT was vertically centered between the metal walls. A large *h/d* ratio ($h/d \approx 1$) creates a relatively large EUT, and conversely a small *h/d* ratio ($h/d << 1$) creates a relatively small EUT.

If a sufficient separation distance exists between the box and metal walls, the currents induced on the box and the localized EM field structure should be similar to those of the free-space simulation. This is due to the diminishing coupling between the box and the metal walls as the separation distance increases. If the separation distance is small, the currents and fields should be significantly altered from that of free-space due to the increased coupling between the box and the walls of the TEM cell. This coupling results in the local excitation of higher-order modes surrounding the EUT. Since below cutoff, the TEM cell propagates only the TEM mode, these higher-order modes do not propagate, but exist as stored energy surrounding the EUT. If sufficient coupling exists between the EUT and the TEM cell walls, the notion that the TEM cell electrically stresses the EUT in a manner similar to that of a free-space environment may no longer be valid.

3. Finite-Difference Time-Domain (FDTD) Simulation

The finite-difference time-domain method was used to numerically simulate the free-space and TEM cell environments. The FDTD method was chosen for this application because it solves Maxwell's equations in the time domain. This offers benefits over frequency-domain methods, such as the Finite-Element Method (FEM) or Method of Moments (MOM), because all frequencies of interest are solved simultaneously.

A Fortran FDTD code was used to simulate the free-space and TEM cell environments diagramed in Figure 3. This code implements Berenger's perfectly matched layer (PML) absorbing boundary condition [17]. The plane-wave TEM mode excitation is applied using a Huygens surface [18]. This surface enables the excitation of a uniform plane wave within the simulation space.

The free-space model, illustrated in Figure 3(a), shows that the metal box is positioned in the center of the simulation model, surrounded by a volume of air. Two boundaries are located along the perimeter of the simulation space. The Huygens surface is the innermost boundary used to source the plane-wave excitation. In both the free-space and TEM cell models, the incident plane wave propagates in the positive x-direction with the electric field tangential to the z-axis. Located a few cells behind the Huygens surface is a PML region 16 cells thick, truncating the computational volume on all sides.

The TEM cell model is identical to that of free space except for the addition of perfectly conducting metal walls that extend along the x-y planes across the top and bottom sides of the Huygens surface. These two walls are used to simulate the septum and lower wall of the TEM cell.

3.1 FDTD Model Parameters

An important parameter when using the FDTD method is determining the cell size (Δx) of the simulation model. The maximum cell size is limited by one of the following two requirements: the cell size must be small enough to resolve both the simulation geometry and the frequencies of interest. Since the geometry being modeled is a square box with a relatively large aperture, the cell size for this situation is limited by resolving the frequencies of interest. This study is generally concerned with the range of frequencies from 9 kHz to 2 GHz. To ensure that sufficient spatial resolution is achieved, at least 10 cells per wavelength are required. In order to be safely within this limit, the cell size is determined by ensuring 20 cells per wavelength at 2 GHz. In addition to ensuring stability at 2 GHz, this also allows for accurate analysis for a range of frequencies up to 4 GHz. In free-space, 20 cells per wavelength at 2 GHz requires a cell size of 7.5 mm. The Courant Stability condition, which ensures the simulation is stable in time, requires a maximum time step (Δt) of 14.4 ps.

3.2 EUT: Square Box With an Aperture

The EUT in this study is represented as a square perfectly conducting metal box with a rectangular aperture on the front surface, as illustrated in Figure 5. A metal box was chosen because it represents a generic EUT of equal size in all three dimensions. This EUT could be realized as modeling an electronic device within a shielded metal case such as a computer. The metal box permits the current flow to be monitored on all surfaces. Fields are able to penetrate through the aperture, allowing field levels both inside and outside the EUT to be examined.

The size of the box was selected to be square, with a length of 20 cells (150 mm) on each side. This size was chosen because it is equivalent to $\lambda/2$ at 1 GHz. At lower frequencies (100 MHz), the box is electrically small compared to a wavelength, and at higher frequencies (1 to 2 GHz), the box's dimensions are comparable to a wavelength. For frequencies above 2 GHz, the box is electrically large. For increasing frequencies over the range of interest, this box size allows for a comparison between the TEM cell and free-space environments for an EUT that is electrically small, comparable, and large compared to a wavelength, respectively. The illustration below diagrams the EUT layout, along with the approximate probe locations where field quantities are monitored.

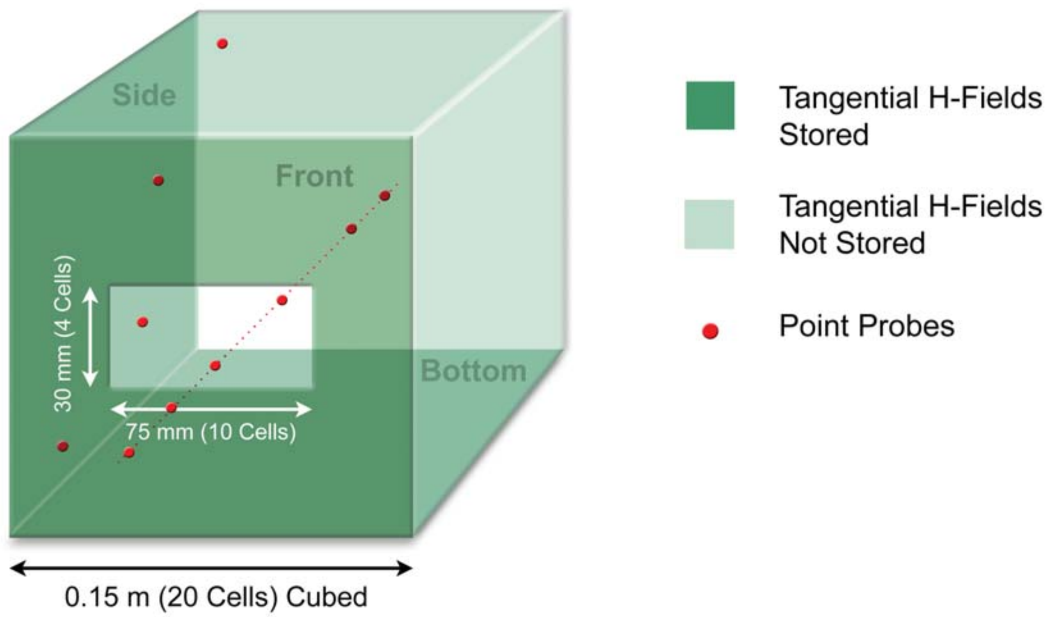

Figure 5: Perspective view of EUT: a metal box with a centered aperture.

As shown in Figure 5, the rectangular aperture is centered on the front surface of the box. To probe the currents on the box surfaces, the tangential magnetic fields were stored at each time step. Since the geometry of the box and the TEM cell walls are symmetric, the currents on the left and top surfaces are respectively identical to those on the right and bottom surfaces. To limit the amount of data collected, the magnetic fields along the back surface were not stored. The z-component of the electric field was stored at 10 probe locations placed inside and outside the box at each time step.

3.3 Plane-Wave Source

A Huygens surface was used to excite a plane wave, propagating in the positive x-direction, into the simulation grid. The plane wave was polarized with the electric field in the positive z-direction (magnetic field in the –y direction). The incident wave has the shape of a Gaussian pulse with a frequency spectrum that includes all frequencies of interest. The two graphs in Figure 6 show, respectively, the z-component of the electric field in time and the frequency spectrum of the waveform.

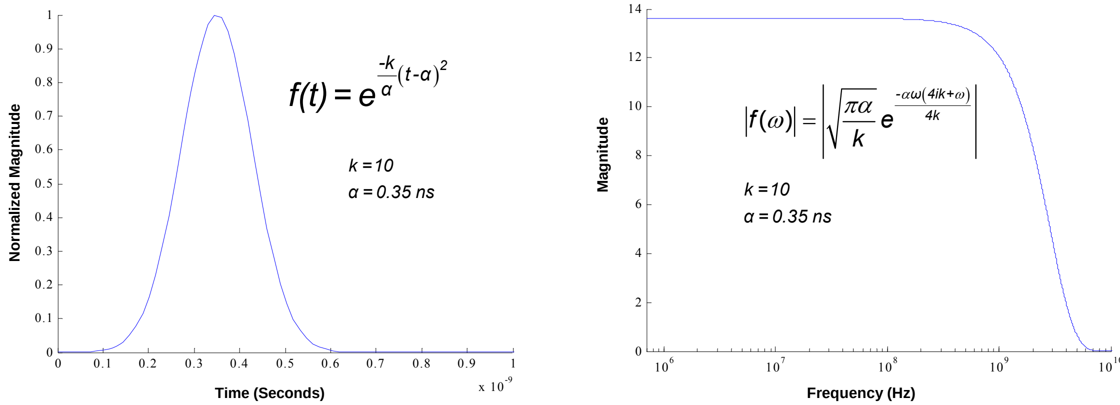

(a) (b)

Figure 6: (a) Time-domain waveform and (b) frequency spectrum of incident pulse.

3.4 Determining Number of Simulation Time Steps

An important aspect of time-domain simulations, especially if frequency-domain analysis is to be performed, is determining the number of time steps required to ensure that the results obtained have the desired accuracy. One potential disadvantage and limitation of a time-domain approach is the requirement that all resonances must be sufficiently attenuated to accurately determine the frequency response of the system. Since the simulation is lossless, energy that enters the box through the aperture resonates for a relatively long duration. This resonance gradually attenuates with time since energy reradiates through the aperture. Since the box has a high Q-factor, many time steps are required to provide accurate results.

For a given amount of processing power, two factors primarily determine the time required for a simulation: the size of the simulation model, and the number of iterations required. Since the number of iterations is an important factor that determines total simulation time, a balance had to be reached between the accuracy of the results and the limited time resources available for simulation. To determine the necessary time steps required for accurate results, the free-space model was simulated for various time steps. For each simulation, the frequency spectrum of an electric field point, centrally located within the box, was calculated. The frequency spectrum of the electric field converged as the number of time steps increases. The electric field in the center of the box was chosen because the resonance of the box creates a sharp peak in the frequency spectrum. Figure 7 shows the frequency spectrum of the internal field value for various simulation time steps. As the number of time steps is increased, the frequency spectrum and the resonant peaks began to converge.

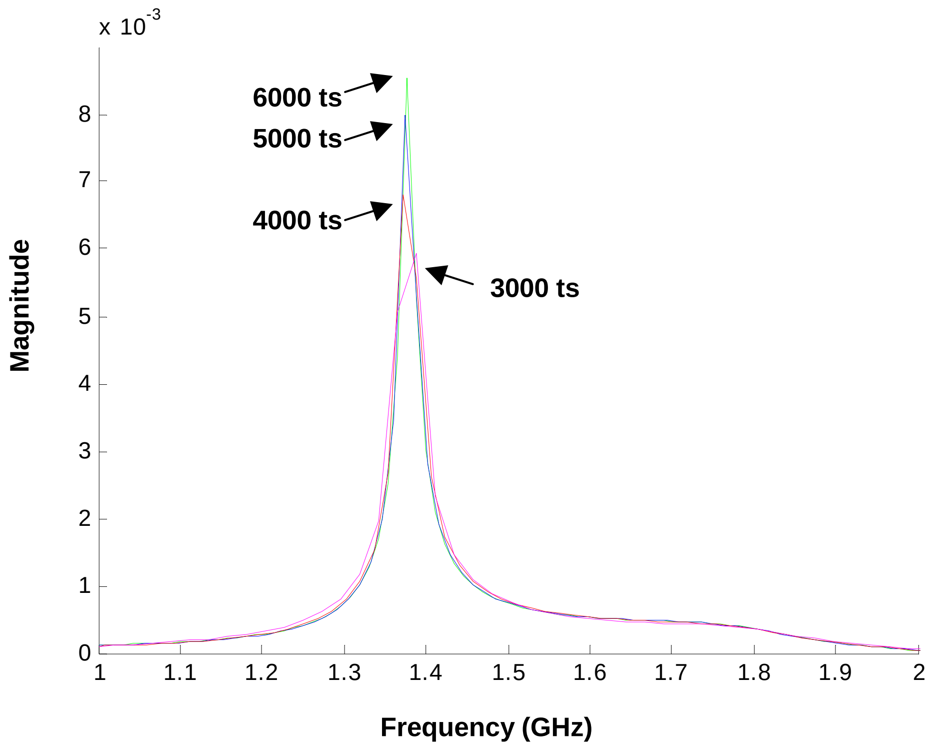

Figure 7: Frequency spectrum of an electric field point centrally located within the box.

It was determined that 6000 time steps ensure sufficiently accurate results, and provide a balance between accuracy and the finite time resources available. The simulation time required for the TEM cell model varies in proportion to the distance (*d*) between the metal walls. As this distance is increased, the simulation size of the model enlarges, lengthening the simulation time.

4. Free-Space Simulations

Data collected from the simulation of the free-space model provided the reference case. The TEM cell models were then compared to this reference. Figures 8(a-f) show a cross section of the electric field distribution, and the currents induced on the box at three successive time steps.

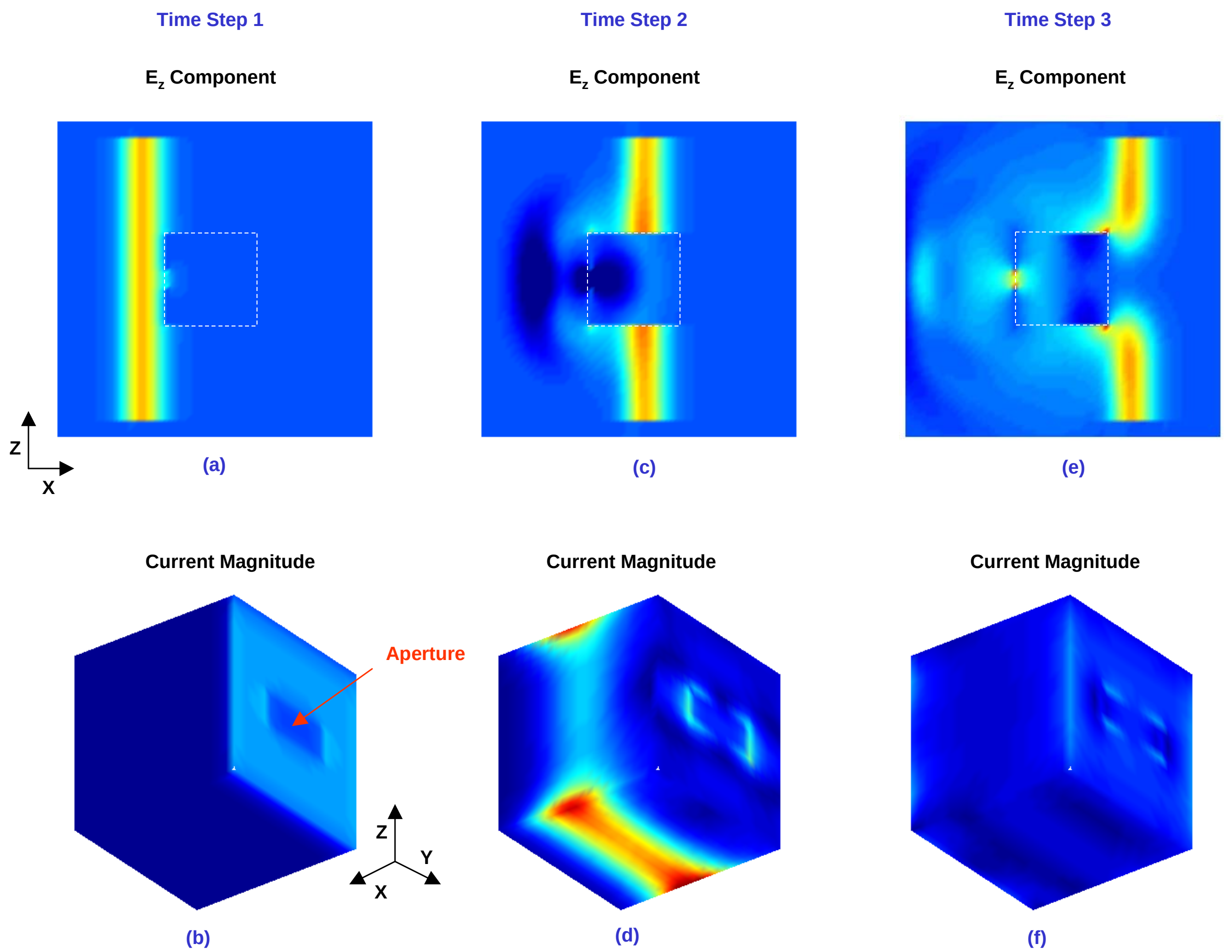

Figure 8: Cross section of the electric field (a,c,e) and perspective view of the current magnitude (b,d,f) for the free-space model.

A cross-sectional slice of the z-component of the electric field for three different times steps is displayed in Figures 8(a,c,e). The white dotted lines outline the location of the box. The bottom three figures show the magnitude of the current distribution on the box at time steps corresponding to the figures above. Figures 8(a,c,e) were produced by storing the z-component of the electric fields along a x-z plane bisecting the center of the box in the y-direction. The current plots were generated by storing the tangential magnetic field components adjacent to the outside metal walls of the box. The magnitude of this current was determined by the two tangential component vectors at each cell location along the box sides.

The upper three images in Figure 8 display the plane wave propagating in the positive x-direction. At time-step 1, the plane wave is uniform in the z-direction and has a Gaussian profile in the x-direction. At this time step, the incident plane wave begins interacting with the metal box. Along the surfaces of the box, the tangential electric fields are forced to zero, and as a result the box can be seen as a shadow against the approaching plane wave. The lower three images show the distribution of current on the outside of the box at the same instant in time. The plane wave incident upon the front surface of the box induces a current flow along the front surface. The aperture is clearly visible as a darker rectangular region along the front surface.

The middle two figures display the electric field distribution and current magnitude at time-step 2 when the plane wave is passing across the box. The backscatter from the box is seen as a dark blue region in Figure 8(c) that propagates in the negative x-direction, away from the front surface of the box. The plane wave was relatively undisturbed along the top and bottom edges of the simulation space, but severely perturbed inside and around the box. Incident energy that propagated through the aperture is seen inside the box. A large magnitude of current was induced in the areas where the plane wave interacts with the box, as well as around the aperture.

Time-step 3 displays the field distribution and currents induced when the plane wave has passed across the box. The scattered fields propagated away from the box and became absorbed by the surrounding PML. The energy present inside the box resonated within the cavity and slowly reradiated through the aperture. Once the plane wave passed across the box, the currents induced on the outside surfaces reduced and further diminished with time.

5. TEM Cell Simulations

The TEM cell models were similar to the free-space model with the addition of two perfect electrically conducting metal walls along the top and bottom surface of the simulation space. These walls were introduced by forcing the tangential electric fields (x and y-components) on the walls to zero. Proper positioning of the metal walls was required to ensure that they do not interfere with the Huygens surfaces or the PML regions.

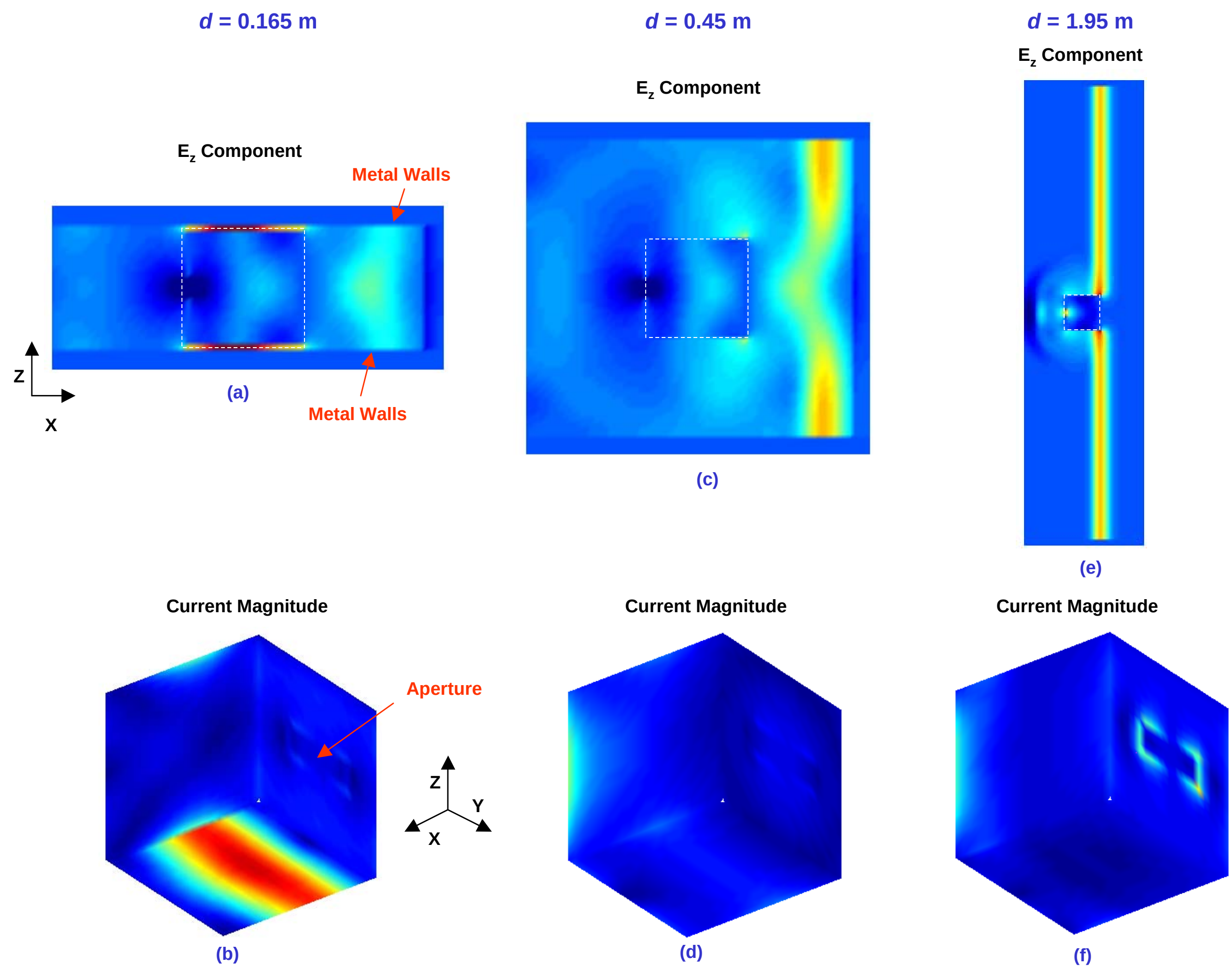

Figure 9: Cross section of the electric field (a,c,e) and perspective view of the current magnitude (b,d,f) for various TEM cell models with $h = 0.15$ m.

A cross-sectional slice of the z-component of the electric field for several different sized TEM cell models are shown in Figures 9(a-f). The upper three figures (a, c, e) display the z-component of the electric field for TEM cells of different dimension d. The lower three figures (b, d, f) show the magnitude of the induced current density on the box corresponding to the time steps above. The leftmost two figures (a and b) display the electric field and current density when the distance separating the top and bottom sides of the box and the TEM cell walls is 1 cell length ($d = 0.165$ m). This is an extreme case when the box represents the largest EUT size possible in the TEM chamber. The areas in red represent the areas of greatest magnitude of electric field and are seen in this case to be located between the top and bottom surfaces of the box and the metal TEM cell walls. The blue areas, along the top and bottom regions of each simulation space, indicate that the magnitude of the z-component of the electric field is zero. The metal walls of the TEM chamber prevent any electric fields from penetrating into these areas. Due to the large EUT size shown in Figure 9(a), the majority of the incident plane wave was reflected back in the negative x-direction. The transmitted wave, shown to the right of the box, has a reduced magnitude due to the large EUT size. Intense electric fields remained present between the box and the TEM walls even after the plane wave has passed by. This indicates that strong coupling existed between the box and the TEM walls.

A case where the distance between the metal walls is increased to $d = 0.45$ m is shown in Figures 9(c and d). Since the box itself has a length of $h = 0.15$ m in each direction, the depiction here represents the case when the EUT size is one-third the separation of the metal walls. Again, the metal walls of the chamber block all electric fields along the top and bottom edges of the simulation space. As a result, any scattered fields from the box propagating toward the top or bottom metal walls reflect back into the simulation space. The extent of coupling existing between the metal box and the TEM wall is not apparent in Figure 9(c).

In Figures 9(e and f), the distance between the metal walls is $d = 1.95$ m. Although the size of the box remains unchanged, it appears smaller in proportion to the large model size in the z-direction. Figure 9(e), shows the incident plane wave and the local scattering around the box. If the distance between the metal walls of the TEM chamber and the box is relatively large, it could be expected that the currents induced on the box by the plane wave would be similar to those of the free-space case.

6. Data Comparison: Free-Space and TEM Cell

The free-space and TEM cell models were simulated and the data collected from the various probes were stored for post-processing. To compare the free-space and TEM cell simulation results, the time-domain data collected from the simulations were converted into the frequency domain. Transferring the data into the frequency domain decomposes the time-domain data into its frequency content. For this application, comparing the frequency content of the data allows for a more thorough comparison than a time-domain approach.

The data were evaluated by comparing the currents induced on the box in the frequency domain. To achieve this, each component of the tangential magnetic fields, adjacent to the outside surfaces of the box, was transformed into the frequency domain. This was accomplished by applying a Fast Fourier Transform (FFT) algorithm to the waveform that resulted from storing the magnitude of a particular magnetic field component at each time step. Transforming the time-domain waveform of a particular component into the frequency domain resulted in a complex quantity for each frequency obtained. The frequency range and resolution depend on the sampling frequency and number of samples of the original time-domain data. Each component was transformed separately and its value, in this study, was obtained by taking the real part of the complex frequency content at the particular frequency of interest. This is carried out on both components representing the current vector. The magnitude of the resulting vector was then taken. This procedure was repeated for each cell along the shaded surfaces, shown in Figure 5.

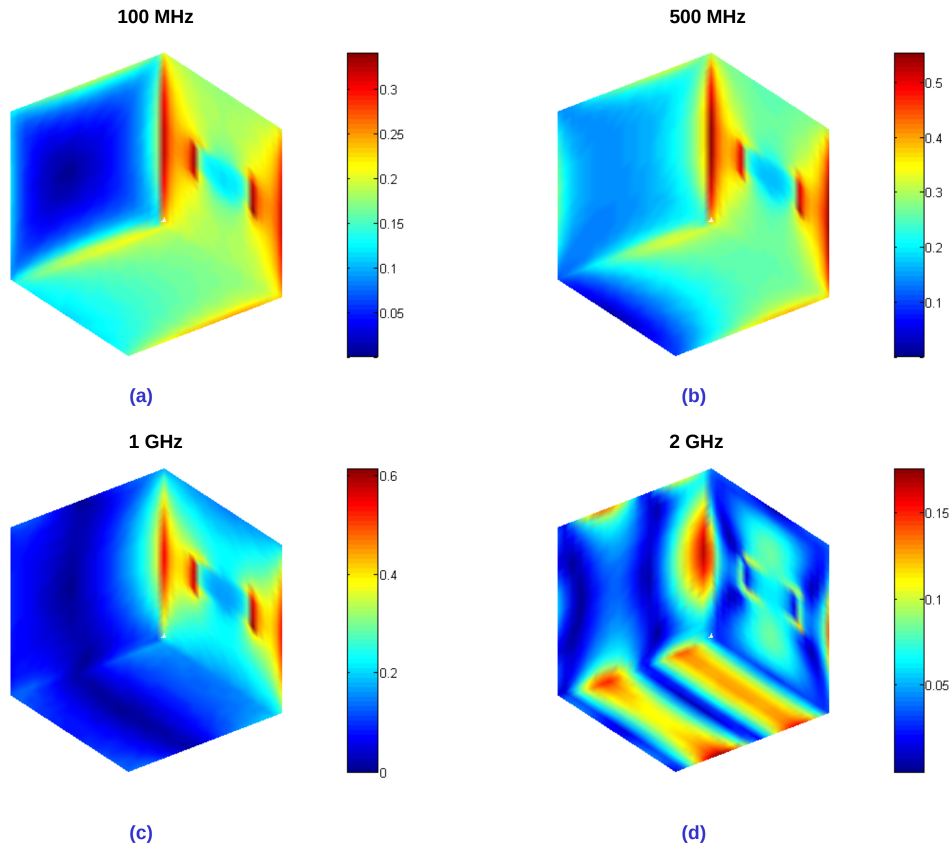

Figure 10: Free-space current magnitude at various frequencies for h = 0.15 m.

Figure 10(a-d) displays the current magnitude at various frequencies for the free-space model. Shown are cutaways of the box illustrating the current on the outside surfaces. Figure 10(a) displays the magnitude of the current distribution at 100 MHz. At this frequency, the box is electrically small compared to a wavelength. The magnitude of the current is primarily uniform over the front and bottom surfaces with increases in magnitude evident along the edges and around the aperture. The magnitude of the current along the side surface is greatest along the four edges and diminishes towards the center. The distribution at 500 MHz is shown in Figure 10(b), where the box length is $\lambda/2$. Figure 10(c) displays the distribution at 1 GHz, where the box length is equal to a wavelength. For this case, a full wavelength taper in current magnitude is evident across the bottom surface. Figure 10(d) shows the distribution at 2 GHz, a frequency for which the box is considered electrically large. At this frequency, the current is seen to vary in magnitude across all three surfaces. Two wavelengths are visible in the taper of current magnitude across the bottom face. Along the two remaining surfaces, the distribution of current is also noticeably different compared to the distributions at lower frequencies.

Similar post-processing was performed on the TEM cell models. The current distributions from the TEM cell model with *d = 0.3* m is shown in Figure 11(a-d). Slight variations are noticeable when comparing the current distributions of the TEM cell models to that of the free-space model.

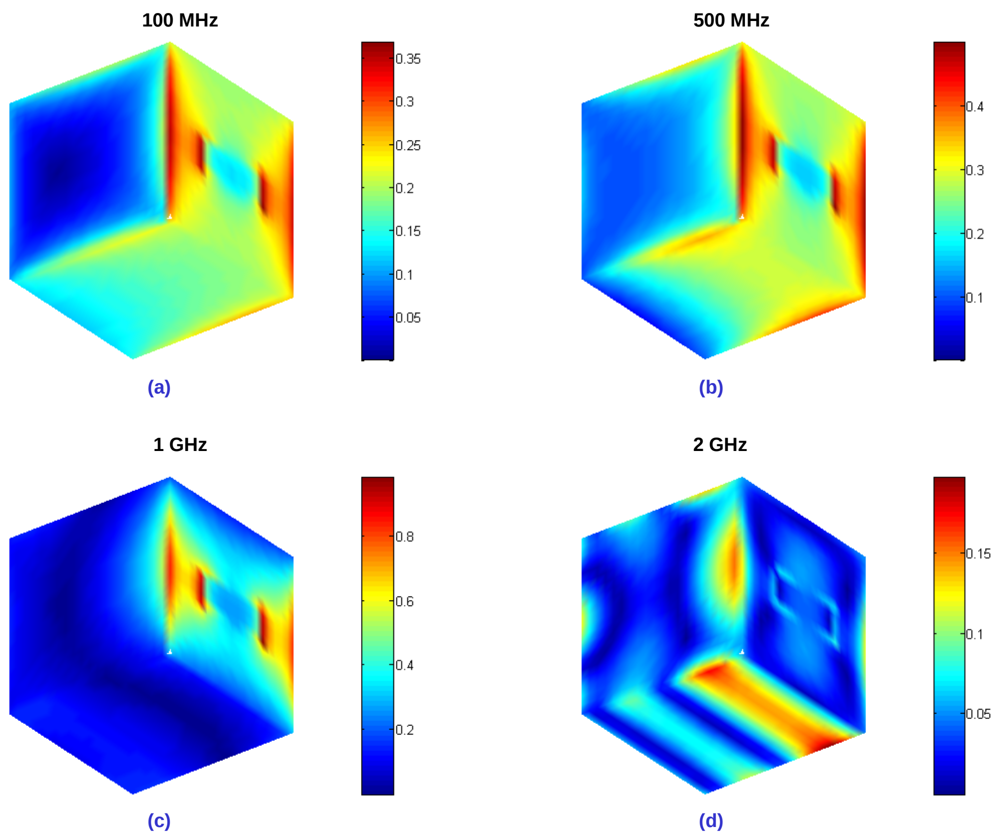

Figure 11: Current magnitude at various frequencies for the TEM cell model with d = 0.3 m and h = 0.15 m.

7. Correlation Algorithms

To quantitatively compare the current distributions of the TEM cell and free-space models, a correlation algorithm had to be developed. Ideally, the correlation algorithm should result in a single value describing the extent to which they relate. After the free-space model is compared to all TEM cell models of varying dimension *d*, the correlation number could be plotted as a function of metal wall separation (*d*). Depending on the results, this plot should provide criteria for determining for what separations the TEM cell replicates the free-space environment. The following section describes several algorithms employed to correlate the data.

7.1 Simple Difference

The first correlation algorithm applied took the average difference between the current values of the free-space and the TEM cell model at each cell location along the sides of the box as described by equation (1):

$$\Delta_{sd} = \frac{\sum_{i=1}^{N}\left(\left|\left|\vec{J}_{fs}^{i}\right| - \left|\vec{J}_{tem}^{i}\right|\right|\right)}{N}. \tag{1}$$

In this equation, $\left|\vec{J}_{fs}^{i}\right|$ is the magnitude of the free-space current for a specific frequency at cell location ***i***. $\left|\vec{J}_{tem}^{i}\right|$ is the magnitude of the corresponding TEM cell current at the same frequency and location, and ***N*** is the number of cells on each surface.

Equation (1) is an inadequate correlation algorithm because the difference is not normalized to the magnitude of the numbers. For example, two small numbers could differ by as much as 100 percent, but the absolute difference would produce a negligible result. On the other hand, two large numbers could differ by only 0.1 percent, but due to the magnitude of the numbers, the absolute difference could still be significant.

7.2 Percent Difference

To normalize the difference to the magnitude of the numbers, the following percent difference formula was utilized:

$$\Delta_{pd} = \frac{\sum_{i=1}^{N}\left(\frac{\left|\left|\vec{J}_{fs}^{i}\right| - \left|\vec{J}_{tem}^{i}\right|\right|}{\left|\vec{J}_{fs}^{i}\right|}\times 100\right)}{N}. \tag{2}$$

Equation (2) was applied to numerous TEM cell models of various dimension *d*. The results of the percent difference as a function of separation (*d*) are shown below in Figures 12(a-c).

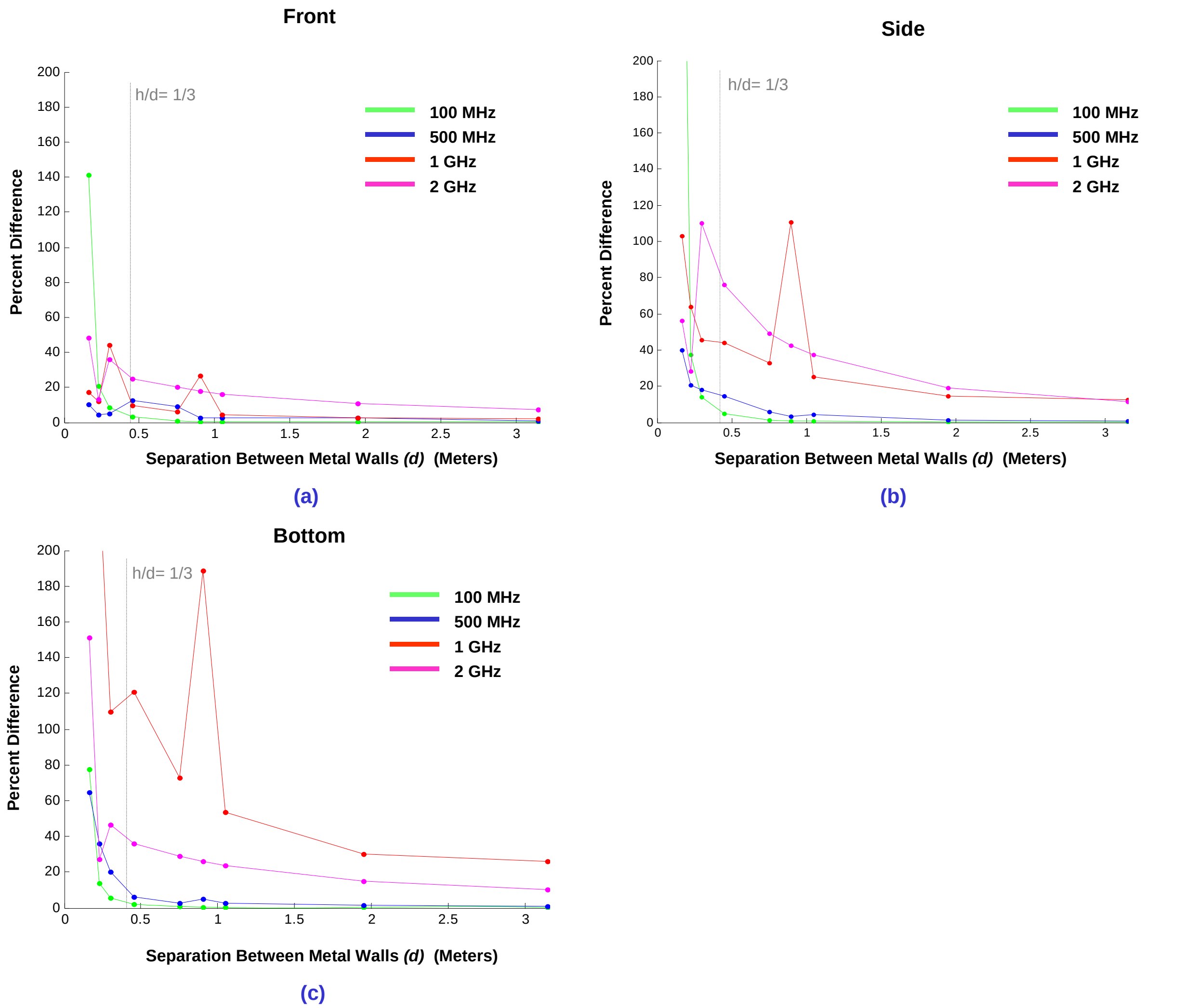

Figure 12: Percent difference for various separations along the (a) front, (b) side, and (c) bottom surfaces of the box for h = 0.15 m.

The three surfaces of the box were analyzed individually. For each TEM cell model, the percent difference was computed at four frequencies. The green curves in the graphs show the percent difference between the free-space model and the TEM cell models at 100 MHz. At this frequency the box is electrically small, and for all three surfaces the percent difference quickly declines as d is increased. The curves representing 500 MHz and 2 GHz show the same trend. However, the percent difference is significantly greater over the range of separations at 2 GHz. At 1 GHz, a frequency at which the box is comparable to a wavelength, the percent difference over the range of separations is also noticeably large. At certain separations, such as d = 0.9 m, the percent difference is dramatically increased. This increase is most significant along the bottom surface (Figure 12(c)) where the percent difference increases from approximately 70 to 190 percent. A vertical line is included in Figures 12(a-c) representing the position along the x-axis when $h/d=1/3$ corresponding to the 1/3 rule. Significant increases in percent difference are still evident when $h/d < 1/3$ (d > 0.45 m). To verify that the spikes are due to changes in the current magnitude, and to qualitatively visualize the disparity, Figure 13(a-d) displays the current magnitudes along the bottom surface at 1 GHz for free-space and TEM cell models with *d* = 0.75 m, *d* = 0.9 m, and *d* = 1.05 m.

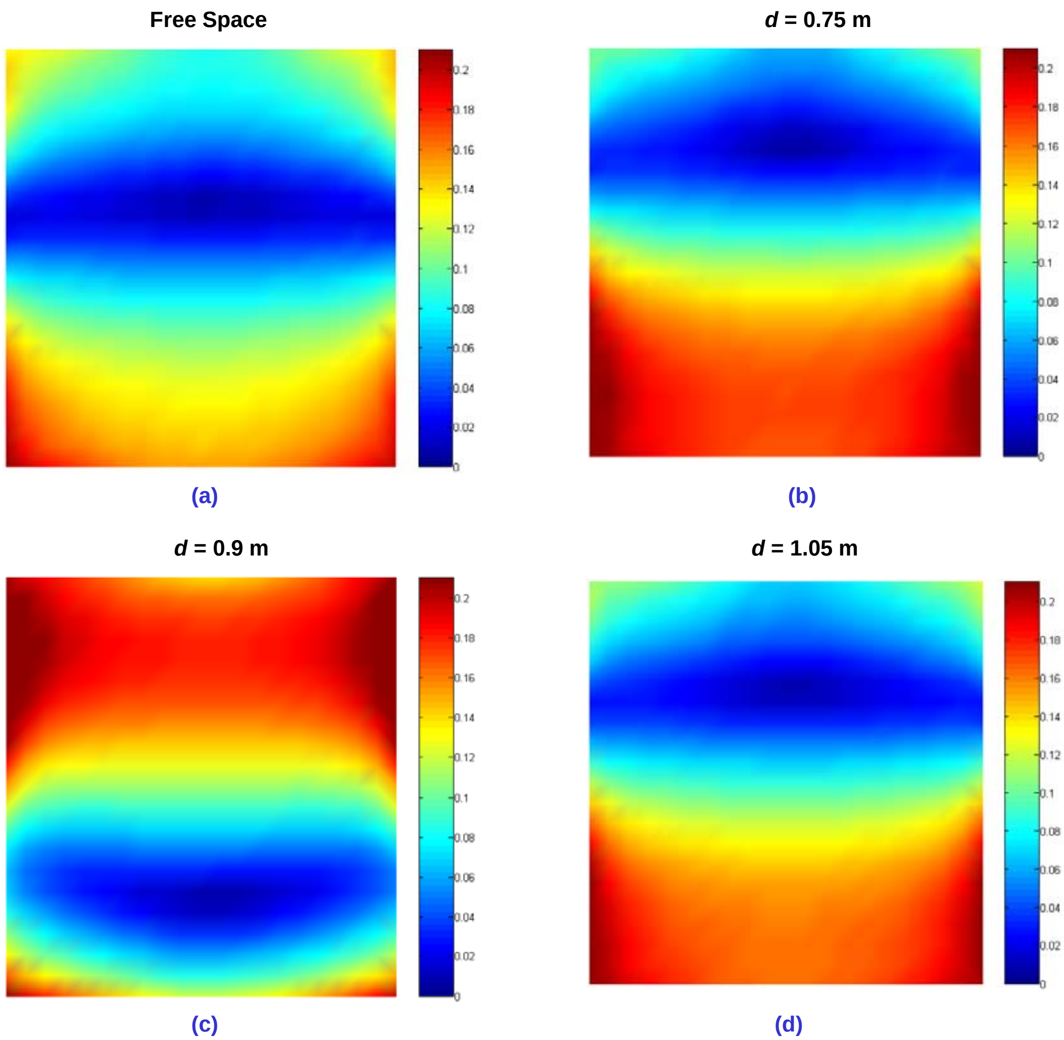

Figure 13: Bottom surface current magnitude at 1 GHz for (a) free-space and TEM cell models with (b) *d* = 0.75 m (*h/d* = 0.2 m), (c) *d* = 0.9 m (*h/d* = 0.17 m), and (d) *d* = 1.05 m (*h/d* = 0.14 m).

Equal color scales are used on all plots in Figure 13. Comparing the free-space plot to the *d* = 0.75 m cell model, Figures 13(a and b), the overall magnitudes of the currents are similar although some variations exist. Figure 13(c) reveals the distribution at *d* = 0.9 m, the separation for which the peak in the percent difference is observed. Comparing Figures 13(a and c), a significant difference clearly exists between the current magnitudes of free-space and the *d* = 0.9 m TEM cell models. Further increasing the separation to *d* = 1.05 m (Figure 13(d)), results in a current magnitude once again similar to that of free space. These results indicate that the current magnitudes for the TEM cell at 1 GHz are significantly perturbed from those of free space when a separation of $d = 0.9$ m exists between the box and TEM cell walls.

7.3 Interactions of a Periodic Structure

A possible explanation of this result is that the observed behavior results from interactions of a periodic structure. Using the method of images, the metal walls, present above and below the box, could be equivalently replaced by an infinite array of images as illustrated in Figure 14. An integral equation formulation of an object in a parallel-plate waveguide is included in the appendix. This formulation shows that a resonance occurs when $d = m\lambda$, where d is the separation of the walls, m is a positive integer, and λ is the wavelength of the corresponding resonant frequency.

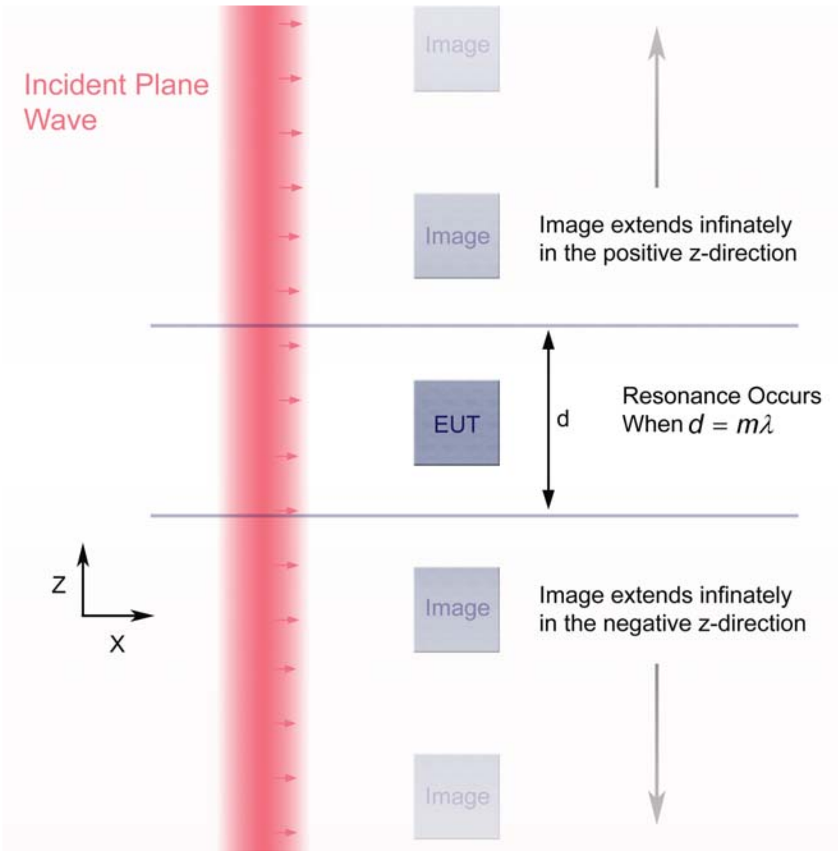

Figure 14: Equivalent periodic array using method of images.

To provide additional data points, further simulations were performed. If the effect is due to certain ratios between the wavelength and image separation, it might also be evident at $d = 0.6$ m and $d = 1.2$ m. Simulations at $d = 0.825$ m and $d = 0.975$ m were also performed to better define the observed spike at 1 GHz for the case of $d = 0.9$ m.

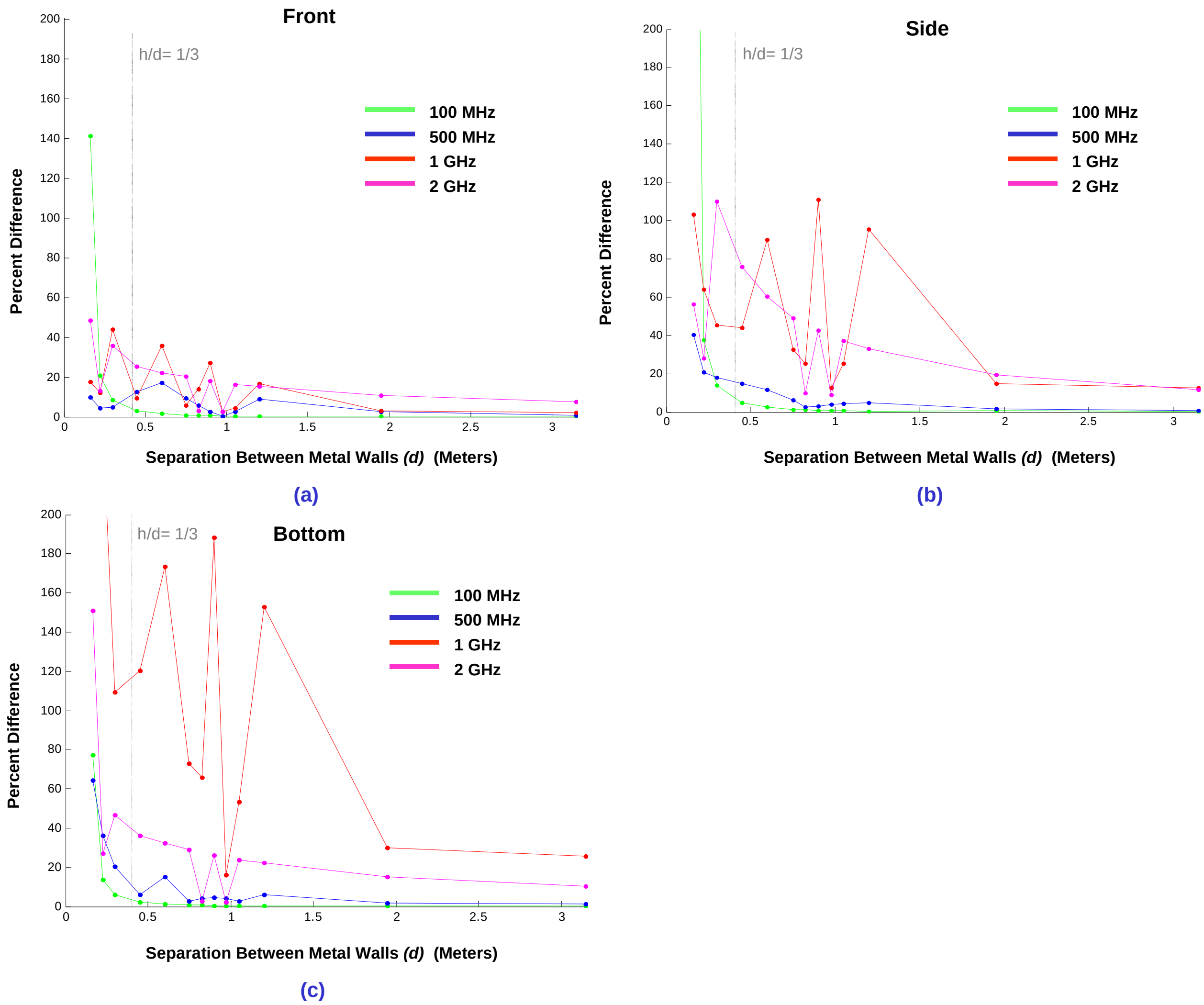

Figure 15: Percent difference for various separations along (a) front, (b) side, and (c) bottom surfaces for h = 0.15 m.

With the additional data points included, the increase in percent difference observed when d = 0.9 m is also evident at d = 0.6 m and d = 1.2 m. The percent difference at d = 0.825 m and d = 0.975 m are reduced in value compared to those for d = 0.9 m, indicating the observed spikes are narrow. The new data points also show an effect at 2 GHz, where the percent difference is actually reduced. A slight increase in the percent difference is also noticeable for d = 0.6 m at 500 MHz. These data support the theory that in certain situations, periodic effects due to the TEM cell environment perturb the currents that would otherwise result in free space.

These data provided evidence that a resonance is occurring for certain cell geometries. However, the degree to which the resonance perturbs the current from free space could be exaggerated in equation (2), due to the division of the difference in current by the magnitude of the free-space current. If the free-space current magnitude at a cell location is infinitesimally small, the division will result in a value exceptionally large. An algorithm that might provide better results, by avoiding division by an infinitesimal value, will be investigated.

7.4 Standard Deviation

A correlation algorithm that computes the standard deviation between the free-space and TEM cell data is applied by use of equation (3):

$$\Delta_{sd} = \left(\frac{1}{n-1} \sum_{i=1}^{n} \left(x_i - \bar{x} \right)^2 \right)^{\frac{1}{2}}, \quad \text{where } x_i = \frac{\left| \vec{J}_{tem}^{\,i} \right|}{\left| \vec{J}_{fs}^{\,i} \right|}, \quad \text{and } \bar{x} = \frac{1}{n} \sum_{i=1}^{n} x_i \text{ or } 1. \tag{3}$$

To determine the standard deviation of the two data sets involved (free-space and TEM cell), x_i is taken to be the ratio of the TEM cell model's current magnitude to that of the free-space model at a particular frequency and cell location ***i***. In computing the standard deviation, data from the three surfaces of the EUT were combined, unlike the computation for percent difference, where each side was computed separately. Two slightly different forms of the standard deviation were used. For the first case $\bar{x}$, the average value of the data set was taken to be the mean ratio of current magnitudes. The second case assumes a mean value of 1, since ideally if $\left| \vec{J}_{tem}^{\,i} \right| = \left| \vec{J}_{fs}^{\,i} \right|$ for all i, the ratio is identically 1. This case would compute the standard deviation of the data set from the ideal case of equality.

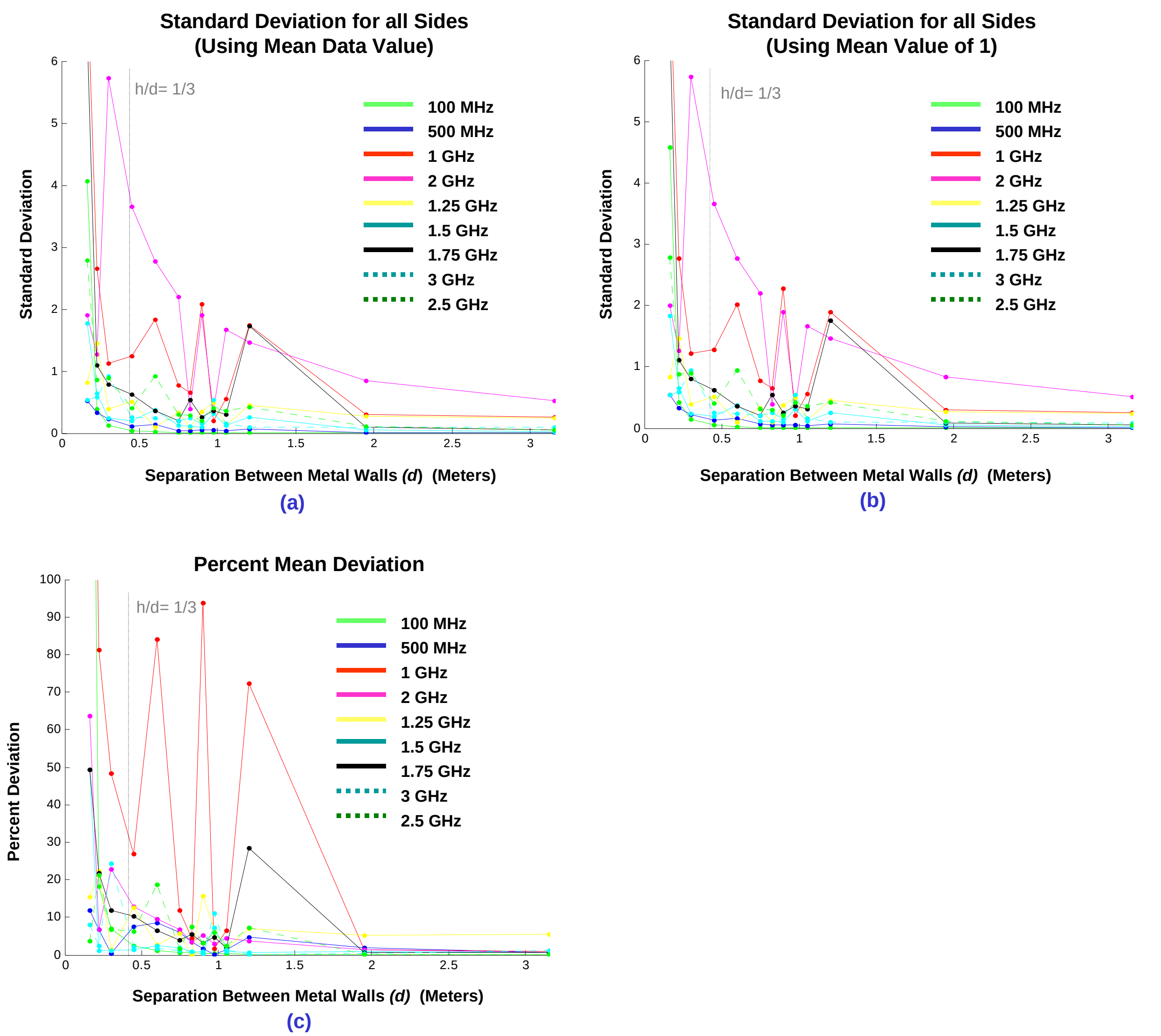

Figure 16: Standard deviation for all three surfaces for $h = 0.15$ m using the (a) mean data value, (b) mean value of 1. (c) Percent mean deviation.

Analysis of the data using the standard deviation algorithm produced the results shown in Figure 16. Using the mean data value in the computation of the standard deviation resulted in the curves shown in Figure 16(a). Similar to the percent difference calculations at 1 GHz, increases in standard deviation are noticeable at $d = 0.6$ m, $d = 0.9$ m, and $d = 1.2$ m. In addition, at 2 GHz the standard deviation is considerably reduced at $d = 0.825$ m and $d = 0.975$ m, a characteristic also evident in the analysis using percent difference. Dissimilar results are also evident when interpreting the data between using percent differences and standard deviation. Compared to the curves of Figure 15(a-c), using percent difference, the spikes observed in the 1 GHz curve have been reduced and are similar in magnitude to the values at 2 GHz. Additional frequencies were included in these plots to determine whether the increases in standard deviation at 1 and 2 GHz are truly due to resonant behavior. Over the range of separations, these additional frequencies have standard deviations generally well below those for 1 and 2 GHz.

The standard deviation of the data from the ideal mean value of 1 is shown in Figure 16(b). The curves produced using this formulation of the standard deviation are very similar to those produced using the mean value of the data (Figure 16(a)). Slight differences are noticeable between the 1 and 2 GHz curves at $d = 0.9$ m and $d = 1.2$ m.

To determine the extent to which the mean data value varies from 1, the percent mean of the ratio is plotted as a function of cell separation. Equation (4) describes the computation of the percent mean:

$$\bar{x}_{\%} = \frac{\bar{x} - 1}{1} \times 100, \text{ where } \bar{x} = \frac{1}{n}\sum_{i=1}^{n} x_i \text{, and } x_i = \frac{\left|\vec{J}^{\,i}_{tem}\right|}{\left|\vec{J}^{\,i}_{fs}\right|}. \tag{4}$$

In equation 4, $\bar{x}_{\%}$ indicates the percent by which $\bar{x}$ deviates from 1, the ideal value if $\left|\vec{J}^{\,i}_{tem}\right| = \left|\vec{J}^{\,i}_{fs}\right|$ for all ***i***. The percent mean ratio, shown in Figure 16(c), indicates the same resonant behavior seen in the percent difference and standard deviation plots. The percent mean ratio is found to be significantly greater at 1 GHz than for all other frequencies.

The percent difference and standard deviation algorithms correlated the current magnitudes for the TEM cell and free space models at various frequencies. Current flow has a direction, and is therefore described at a point by a vector quantity. Since currents on the surfaces of the box flow in planes, the current vectors are decomposed into two components on the FDTD grid. For instance the current flowing on the front surface of the box flows within in a y-z plane. The current vector at each grid point has a y- and z-component. When transferring the current vectors into the frequency domain, each component must be transformed individually. Transforming a current component in time results in a complex frequency value. Therefore, both x- and y-components are complex in frequency. For this study, the real parts of the complex component values were used to determine the value of the component in the frequency domain. The total current vector at a particular cell location is determined from these two component values. The magnitude of the current (in frequency) is then determined by the magnitude of this vector. However, by determining the correlation this way the directions of the current vectors are ignored. For example, at certain locations on the box surface, the magnitude of the currents on the TEM cell model could be identical to that of free space; however their directions might differ. If considering only the magnitude of the currents, the two currents would be considered identical, even though, in actuality they differ in direction.

Since each component in frequency has a magnitude and phase by disregarding the imaginary part, information is lost about the current flow. To fully correlate the current flows between the models, all information given by the Fourier transform (magnitude and phase) must be considered for each component.

7.5 Complex Vector Difference

Equation (5) describes an algorithm for correlating the complex data, which results from transforming each component into the frequency domain:

$$\Delta_{vd} = \frac{\sum_{\mathrm{i}=1}^{n} \left| \hat{x}_{\mathrm{i}} - \hat{y}_{\mathrm{i}} \right|^2}{\sum_{\mathrm{i}=1}^{n} \left| \hat{x}_{\mathrm{i}} \right|^2} \quad . \tag{5}$$

In equation (5), $\hat{x}_{\mathrm{i}}$ is the free-space complex frequency value for the i th component and $\hat{y}_{\mathrm{i}}$ is the corresponding TEM cell value and, n is the total number of vector components along one surface of the box (i.e., 2 times the number of cells on the face). For a specific component, the difference between the complex values resulting from the FFT of the free-space and TEM cell models is computed at a specific frequency. This difference results in a complex number, the magnitude of which is squared. The numerator is the sum of these quantities over all vector components. To provide normalization, the numerator is divided by the magnitude of the free-space component squared. Ideally if $\hat{y}_{\mathrm{i}} = \hat{x}_{\mathrm{i}}$ for all i, the total result equals zero.

Similar to the other algorithms, equation (5) was used to determine the correlation between the data from various trace separations to that of free space. Correlations at four different frequencies were investigated, and the results are shown in Figures 17(a-c). For large trace separations (*d* = 1.95 m and *d* = 3.15 m), the complex vector difference becomes negligible. Over the range of separations, the 100 MHz (green) and 500 MHz (blue) curves indicate a dramatic reduction in vector difference between *d* = 0.165 m and *d* = 0.3 m and remain minimal for separations greater than *d* = 0.3 m. The complex vector difference for the 2 GHz (pink) curve also drops with increasing separation, although the difference is greater on the top surface (Figure 17c). Significant increases in vector difference are evident in the 1 GHz (red) curve, at separations of *d* = 0.3m , *d* = 0.6m , *d* = 0.9 m, and *d* = 1.2 m. The spikes at 1 GHz, previously observed using the percent-difference and standard-deviation metrics, are also evident after computing the complex vector difference. Again, the complex vector difference utilizes all information, including current direction to determine the correlation between the free-space and TEM cell current flows.

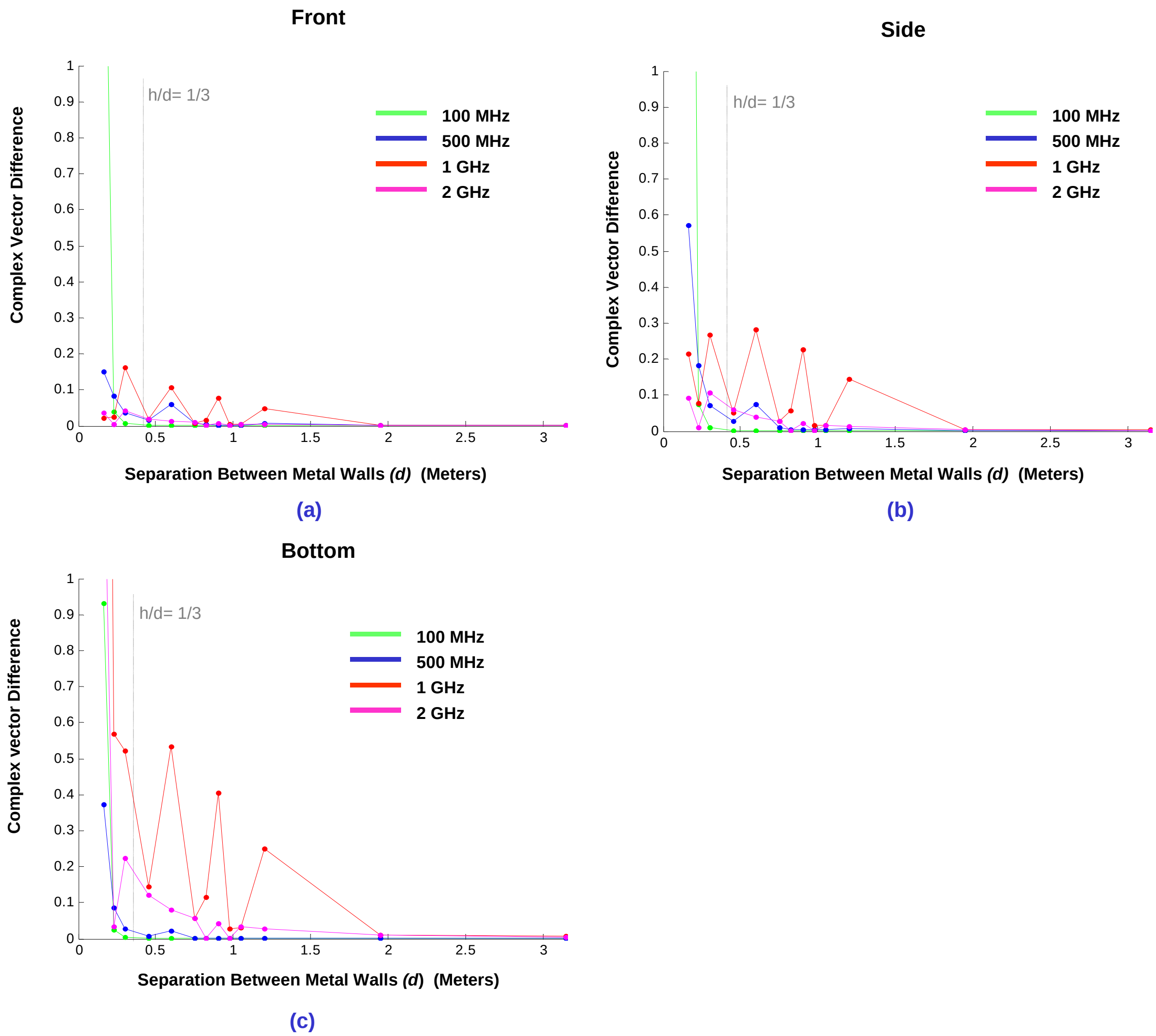

Figure 17: Complex vector difference for h = 0.15 m on the (a) front, (b) side, and (c) top surfaces of the box.

Simulating additional TEM cell geometries of various separations would be useful in better determining the precise location and number of spikes observed in the 1 GHz curve. However, due to the considerable time required for simulation and post-processing, the addition of more data points in the curves above is not practical. If the phenomenon observed at 1 GHz is due to a resonance of a periodic structure, then the effect of the periodic geometry will be highly frequency dependent. A way of obtaining better resolution without further simulation is to compute the complex vector difference over a range of frequencies for a fixed TEM cell geometry. Since the transformation of the time-domain data into the frequency domain reveals its frequency dependence for numerous frequencies, greater resolution can be obtained by correlating the current flows of the free-space and TEM cell geometries over a range of frequencies.

The vector difference between the free-space and specific TEM cell models over the frequency range of interest produced the results shown the Figures 18(a-d), which used separation distances of $d = 0.45$ m, $d = 0.6$ m, $d = 0.75$ m, and $d = 1.2$ m respectively.

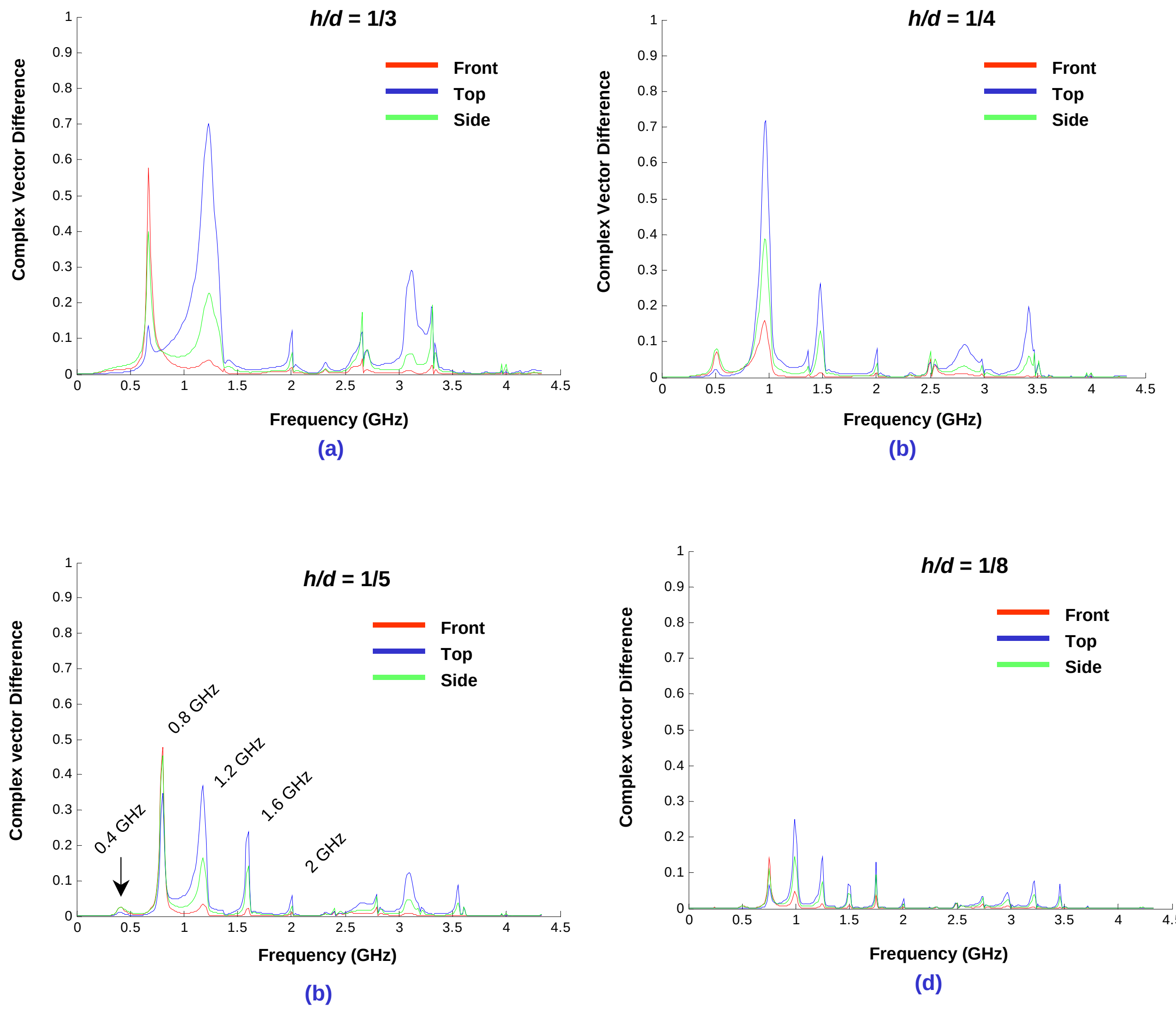

Figure 18: Complex vector difference versus frequency for separations of $d = 0.45$ m, $d = 0.6$ m, $d = 0.75$ m, $d = 1.2$ m in (a-d) respectively for $h = 0.15$ m.

The results in Figure 18(a-d) show that for a specific TEM cell geometry, increases in vector difference occur at multiple frequencies. The dominant frequency, the frequency at which the vector difference is greatest, varies depending on the geometry. The dominant frequencies in Figures 18(b and d) are around 1 GHz. This corresponds to the significant increase in vector difference at 1 GHz seen in Figures 17(a-c). Figures 18(a and c) also indicate dominant and multiple frequencies of increased vector difference. The increases in vector difference for these geometries were not previously seen in Figures 17(a-c) because these frequencies were not included. The spikes in the complex vector difference plots diminish in magnitude and spacing in frequency as the separation distance between the metal walls in the TEM model is increased.

8. Resonance Determined by Plate Separation

Examining the results of Figure 18, the spikes were found to occur at the harmonics of a fundamental frequency. The formulation presented in the appendix shows that this frequency corresponds to the wavelength determined by the separation distance between the metal walls (i.e., $d = m\lambda$). For example, the separation distance (between the metal walls) for the TEM cell model in Figure 18(c) is 0.75 m. In free-space, a wavelength of 0.75 m corresponds to a frequency of 400 MHz. This agrees with the results of Figure 18(c), enlarged and displayed in Figure 19 for convenience. A slight increase is observed at 400 MHz, and the large spikes occur at upper harmonics of this frequency (0.8, 1.2, 1.6 GHz, etc.).

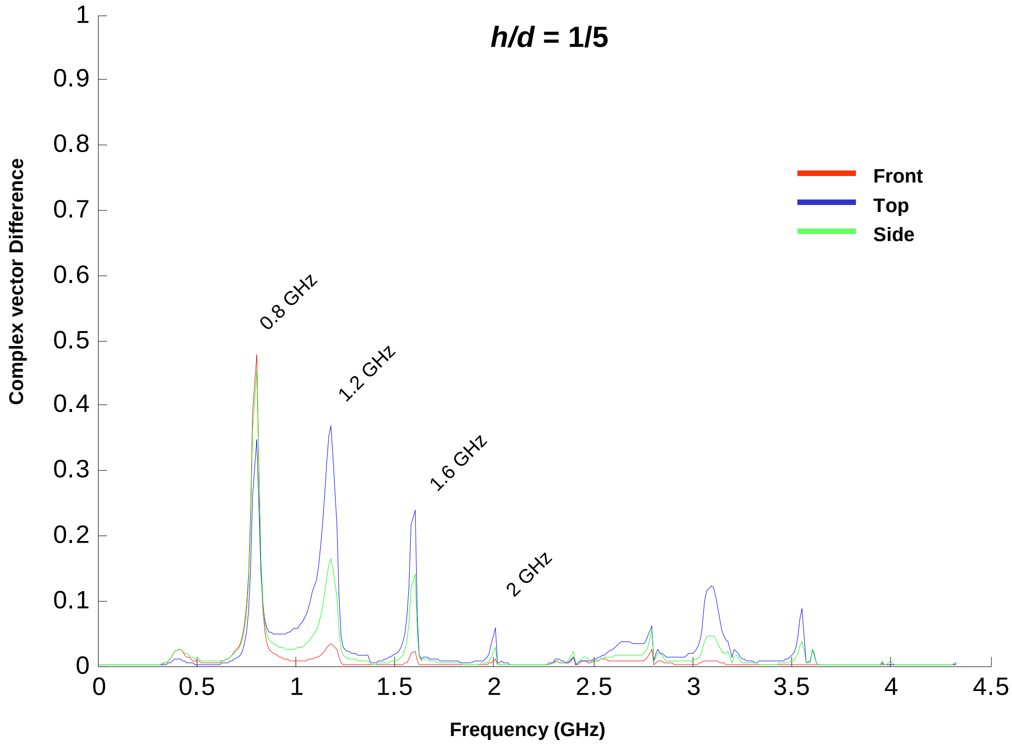

Figure 19: Vector difference between free-space and $d = 0.75$ m TEM cell model for $h = 0.15$ m.

9. Effect of EUT Size on Resonance

The effect of the box's size on the resonance was examined in order to verify that the resonance is due to the separation distance of the parallel walls, and to determine its effect on the resonance. In the following examples, the total wall separation was maintained at d = 0.75 m, and three EUT sizes were investigated: h = 0.075 m, h = 0.15 m, and h = 0.3 m. To determine the vector differences for these cases, the simulation and post-processing codes had to be modified to account for the change in EUT (box) size. For each alteration to the EUT in the TEM cell model, the corresponding free-space simulation had to be performed given that the number of data points differed between the cases.

The results of these examples are displayed in Figure 20. In this figure, cross-sectional slices of the z-component of the electric field are displayed to the left, and the computed vector difference is shown to the right, for the various EUT sizes. The plots of vector difference indicate that the EUT size has the effect of altering which harmonics resonate, but does not influence the fundamental resonant frequency (400 MHz). These results further support the theory, discussed in the appendix, that the resonance is determined by the plate separation.

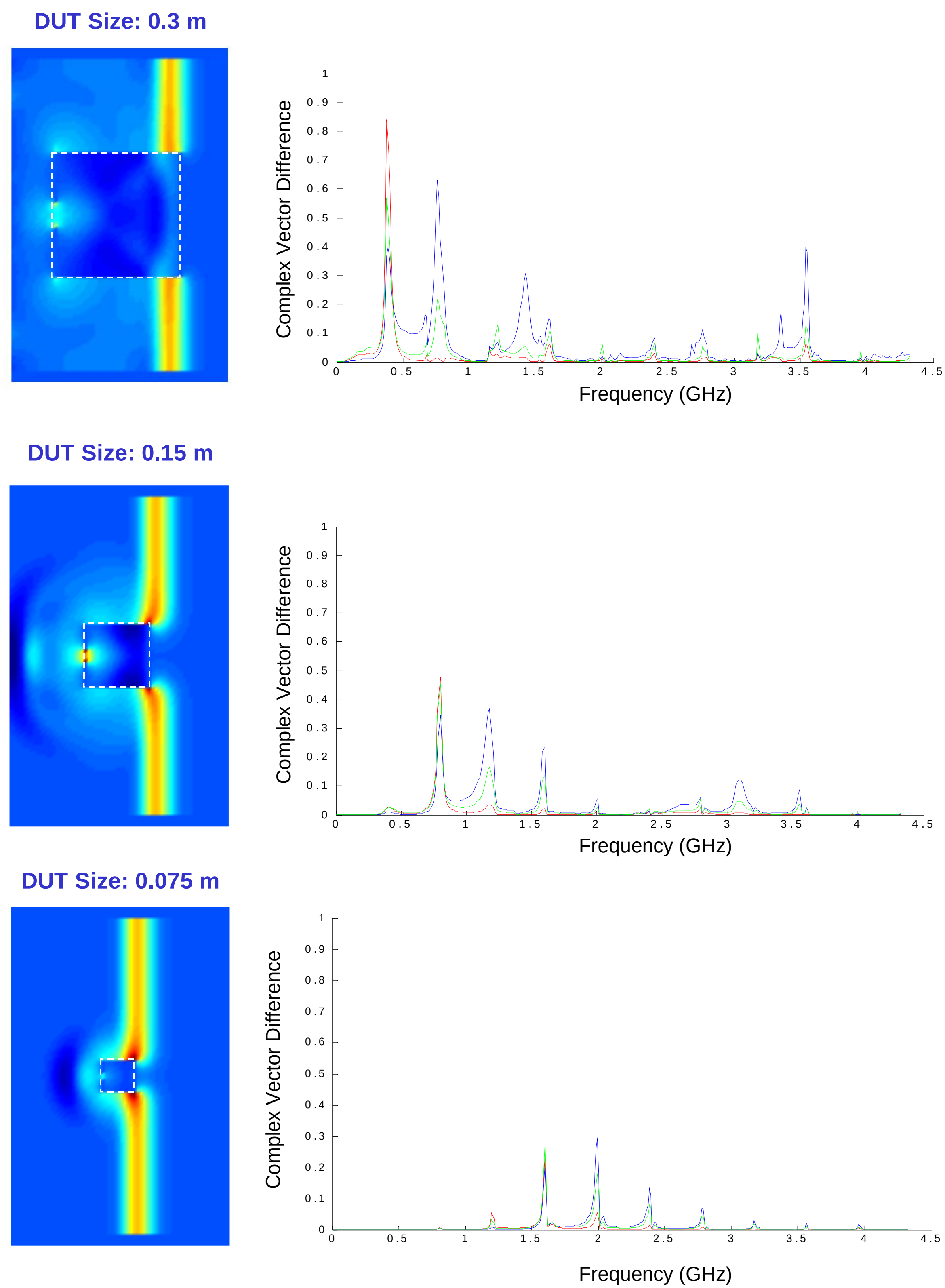

Figure 20: Cross-sectional slice of the z-component of the electric field and the plot of vector difference for a fixed plate separation of d = 0.75 m and box sizes of h = 0.3 m, h = 0.15 m, and h = 0.075 m, respectively.

It is also seen that the wall separation determines the location of the resonances, and that the size of the EUT affects the heights of the resonant spikes. The closer the EUT is to the walls, the more coupling exists between the EUT and the metal walls which perturb the currents from that of free space.

10. Magnetic Field Distribution at Resonant and Non-Resonant Frequencies

At the frequencies for which the vector difference is significantly increased, the currents induced on the outside surfaces of the box were perturbed from that of the free-space environment. If the currents were significantly altered due to a resonance effect, this would indicate that the electric and magnetic field distributions surrounding the box at these frequencies would also be significantly altered from that of the free-space environment.

To visualize the surrounding field distributions at various frequencies, the TEM cell model with a separation distance of d = 0.75 m and a box size h = 0.15 m was investigated. A cross-sectional slice (centered in the y-direction) of the y-component of the magnetic fields was stored at each time step. The data from each point within the slice was converted into the frequency domain, which allows for observation of the field distribution at various frequencies. In Figure 19, the vector difference at 500 MHz is relatively small, and therefore corresponds to a non-resonant frequency. The field distribution of the y-component of the magnetic field, at 500 MHz for free-space and the TEM cell model, is displayed in Figure 21.

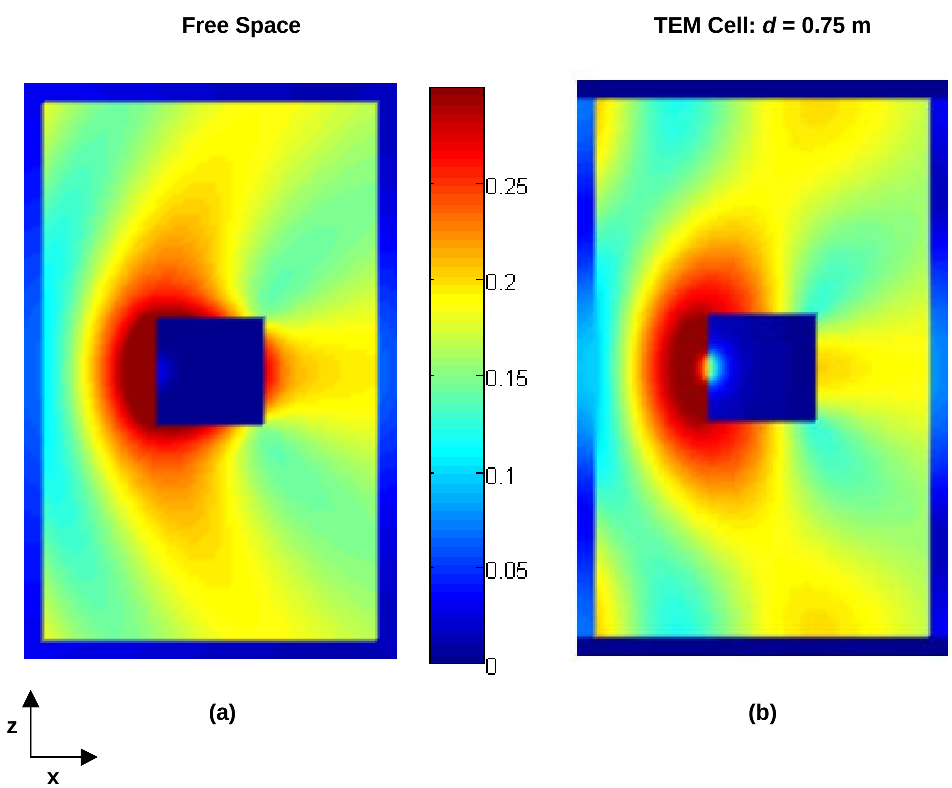

Figure 21: Cross-sectional slice of the magnitude of the y-component of the magnetic field at 500 MHz for (a) free-space model and (b) TEM cell model for h = 0.15 m.

The distribution of the magnetic fields surrounding the box in the TEM model is slightly altered from that of the free-space case. Although differences in the distributions exist, they are generally similar. By observing only the y-component of the magnetic field, the extent that the currents on the box correlate is unclear. The spike in vector difference at 800 MHz signifies that a significant change in induced current distribution occurs at this frequency. The magnetic field distribution at 800 MHz is presented in Figure 22.

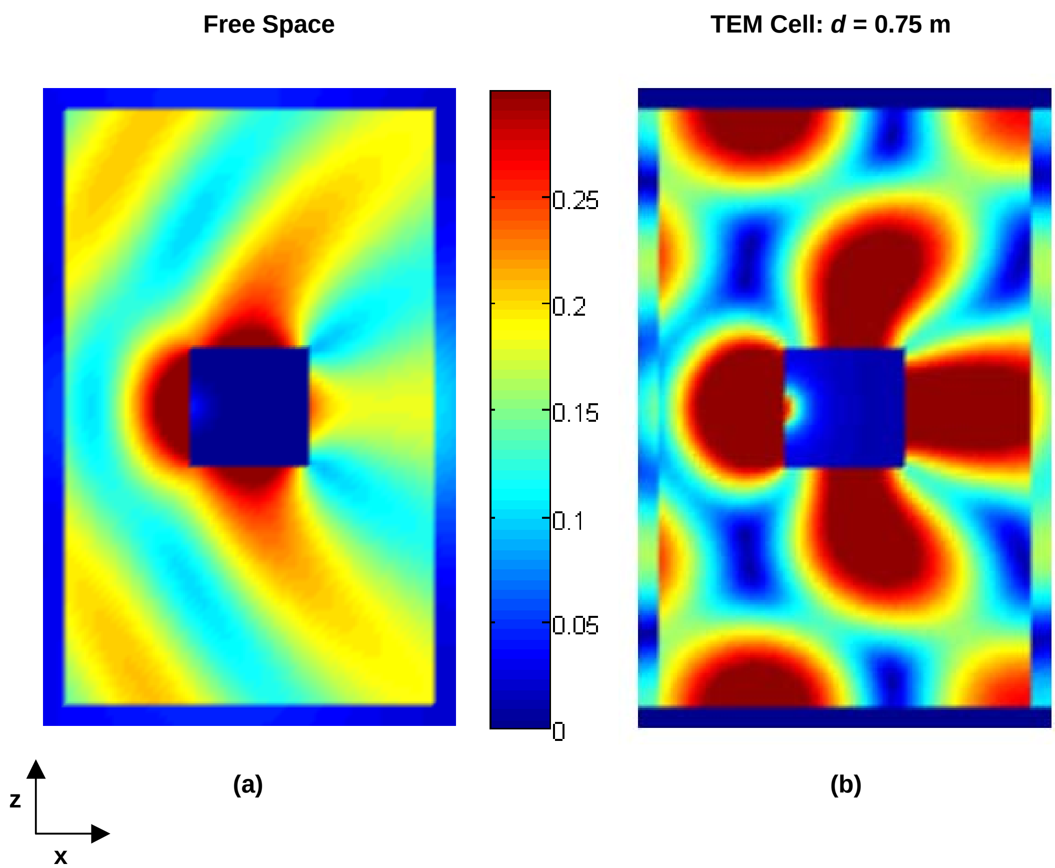

Figure 22: Cross-sectional slice of the magnitude of the y-component of the magnetic field at 800 MHz for (a) free-space model and (b) TEM cell model for h = 0.15 m.

The magnetic field distribution of the TEM cell model at 800 MHz is significantly perturbed compared to that of the free-space model. The resonant effect due to the EUT in a parallel-plate waveguide is clearly visible. The magnitude of the z-component of the electric field along the same plane is also examined. Although differences existed between the free-space and TEM cell models, the resonance is not as pronounced as that observed from the magnetic field.

11. Conclusions

The motivation of the work presented was to examine the performance of a “GTEM” cell for EMC immunity testing. For the “GTEM” cell to be a viable alternative, the electrical stresses induced on a EUT must be comparable to those induced if the test is conducted in a free-space environment. To examine the performance, an identical EUT was modeled in a modified “GTEM” (parallel-plate waveguide) and free-space environment. The effect of relative EUT size with the cell was also investigated.

The currents induced onto the EUT in both environments were examined, and several algorithms were employed to determine how well the currents correlated. The complex vector difference algorithm was determined to be the best metric for correlating the currents induced on the EUT. The correlation results indicated that at certain frequencies, a resonance in the “GTEM” model altered the currents induced on the EUT from that of a free-space environment. The frequencies for which a resonance was found to occur were related to the plate separation d (i.e., $d = m\lambda$). The size of the EUT determines the amplitude and which resonant modes become excited. Resonant frequencies were found to occur even when $h/d < 1/3$.

Future work should determine the influence that the angled septum of a “GTEM” cell has on this resonance. In addition, since EMC testing is concerned with performing measurements, the extent to which the resonances influence measurements needs to be investigated.

12. References

[1] Paul, C. Introduction to Electromagnetic Compatibility. Chapter 2; New York: Wiley Interscience; 1992.

[2] IEC 6100-4-3 Electromagnetic compatibility (EMC)-Part 4: Testing and measurement techniques, Section 4: Radiated, radio-frequency, electromagnetic field immunity test; International Electrotechnical Commission; Geneva; 1996.

[3] Holloway, C. L.; DeLyser, R. R.; German, R. F.; McKenna, P.; Kanda, M. Comparison of Electromagnetic Absorber Used in Anechoic and Semi-Anechoic Chambers for Emissions and Immunity Testing of Digital Devices. *IEEE Trans. on Electromagn. Compat.* Vol. 39, No. 1, 33-47; 1997 February.

[4] Crawford, M. L. Generation of Standard EM Fields Using TEM Transmission Cells. IEEE Trans. on Electromagnetic Compat. Vol. 16, No. 4, 189-195; 1974 November.

[5] Wilson, P. F. Higher-order mode field distribution in asymmetric transverse electromagnetic cells. Radio Science. Vol. 26, No. 2; pp. 551-557; 1991 March-April.

[6] Wilson, P. F.; Ma M. T. Small Obstacle Loading in a TEM Cell. IEEE Int. Symp on EMC; pp. 30-35; 1984 October.

[7] Kim, S.; Nam, J.; Jeon H.; Lee, S. A Correlation Between the Results of the Radiated Emissions Measurements in GTEM and OATS. IEEE Int. Symp. on Electromagn. Compat.: Vol. 2, 1105-1109; Denver, CO; 1998 Aug. 24-28.

[8] Harrington, T. E.; Chen Z.; and Foegelle, M. D. GTEM Radiated Emissions Correlation Testing and FDTD Modeling. IEEE Int. Symp. on Electromagn. Compat.: Vol. 2, 770-775; Seattle, WA; 1999 Aug. 2-6.

[9] Wilson, P. On Correlating TEM Cell and OATS Emission Measurements. IEEE Trans. on Electromagn. Compat.: Vol. 37, 1-16; 1995.

[10] Tsaliovich, A.; Moncion, D.; Okun, A.; Sinfield, D. Using GTEM for Electromagnetic Emission Measurements: Experiments in Test Result Correlation. IEEE Int. Symp. on Electromagn. Compat.: 161-166; Chicago, IL; 1994 Aug. 22-26.

[11] Holloway, C. L.; McKenna, P. M.; Dalke, R.; Perala, R. A.; Devor, C. Time-Domain Modeling, Characterization and Measurements of Anechoic and Semi-Anechoic Electromagnetic Test Chambers. IEEE Trans. on Electromagn. Compat.: Vol. 44, No. 1; 2002.

[12] Boyd, R.E.; Malack, J.A.; Rosenbarker, I.E.; EMI control for data processing and office equipment. In the Proc. of Electromagnetic Compatibility 1975: 1st Symposium and Technical Exhibition on Electromagn. Compat.: pp. 307-313; Montreaux, Switzerland; 1975 May 20-22.

[13] Hill, D.A. Electromagnetic Theory of Reverberation Chambers, National Institute of Standards and Technology Technical Note 1506; 1998 December.

[14] Crawford, M. L.; Koepke, G. H. Design, Evaluation and Use of a Reverberation Chamber for Performing Electromagnetic Susceptibility/Vulnerability Measurements. National Bureau of Standards Technical Note 1092; 1986 April.

[15] Ladbury, J. M.; Koepke, G. H.; Camell, D. Evaluation of the NASA Langley Research Center Mode-Stirred Chamber Facility. National Bureau of Standards Technical Note 1508; 1999 January.

[16] Ladbury J. M.; Koepke, G. H. Reverberation chamber relationships: corrections and improvements or three wrongs can (almost) make a right. IEEE Int. symp. on Electromagn. Compat.; Vol. 1, 1-6; 1999.

[17] Berenger, J. P. A perfectly matched layer for the absorption of electromagnetic waves. J. Computational Phys.: Vol. 114, pp. 185-200; 1994.

[18] Balanis, C. A. Antenna Theory: Analysis and Design. pp. 575-581; New York: John Wiley & Sons, Inc.; 1997.

Appendix: Integral Equation Formulation of an Object in a Parallel-Plate Waveguide

By using an integral equation formulation of a small object in a waveguide, it is possible to understand the behavior of currents and resonances. In general, for an arbitrarily shaped metallic object, the surface current vector $\bar{J}_s(\bar{r}')$, will have an x, y, and z-component. The parallel walls, positioned above and below the metallic object, will produce an infinite array of images of these currents. The following formulation assumes all surface currents have only a z-component, to avoid the complication of solving a dyadic Green's function. This is because the z-components image in the same direction; however, the images of the x- and y-components alternate direction between images. The results of the following formulation should be valid with or without inclusion of these components.

Equation (A1) relates the current on an object (Figure A1) to the electric field at any location in free space [1-5]:

$$\bar{E}(\bar{r}) = \bar{E}^i(\bar{r}) - j\omega\mu\left(1 + \frac{1}{k^2}\nabla\nabla\bullet\right)\oint_S \bar{J}_s(\bar{r}')\, G(\bar{r},\bar{r}')\; dS' . \tag{A1}$$

In this expression $\bar{E}(\bar{r})$ is the E-field at any location, $\bar{E}^i(\bar{r})$ is the incident field, $\bar{J}_s(\bar{r}')$ is the current density on the surface of the perfectly conducting object, $\bar{r}$ is the position of the observation point, $\bar{r}'$ is the position of the source, and $G(\bar{r},\bar{r}')$ is the Green's function, defined below.

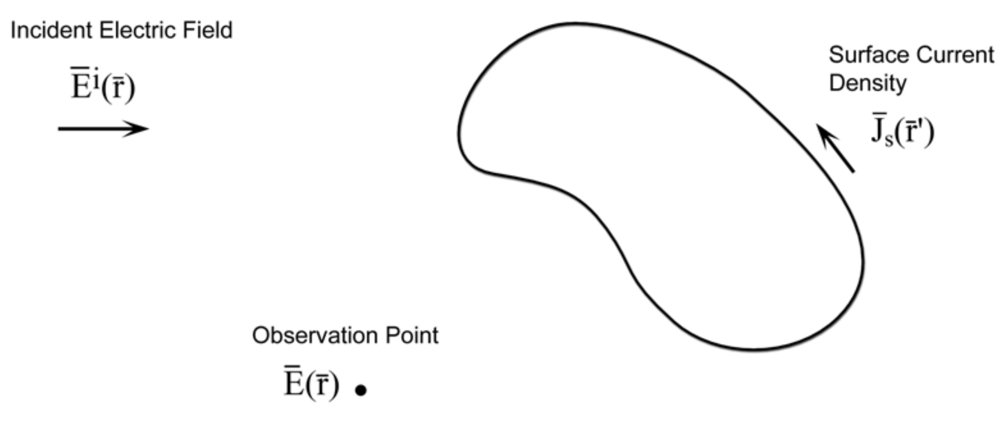

Figure A1: The electric field at any location (observation point) $\bar{E}(\bar{r})$, the incident field $\bar{E}^i(\bar{r})$, and the current density on the surface of a perfectly conducting object $\bar{J}_s(\bar{r}')$.

By forcing

$$\bar{a} \times \bar{E}_{total} = 0 \tag{A2}$$

on the surface of the perfectly conducting object, the integral equation relating the tangential component of the incident field to the current density on the object is given by:

$$\bar{E}^{i}_{\tan}(\bar{r}) = j\omega\mu \left\{ \left(1 + \frac{1}{k^2} \nabla\nabla \bullet \right) \oint_S \bar{J}_s(\bar{r}')\, G(\bar{r}, \bar{r}')\ dS' \right\}_{\tan} . \tag{A3}$$

The expression is often referred to as the electric field integral equation (EFIE). If the incident field is known, the unknown current density $\bar{J}_s$ can be obtained. This equation is known as an integral equation of the *first kind*, since the unknown $\bar{J}_s$ appears only under the integral sign.

If the object is in free-space, then the following three-dimensional free-space Green's function is used:

$$G(\bar{r}, \bar{r}') = G_{fs}(\bar{r}, \bar{r}') = \frac{e^{-jkR}}{4\pi R}, \tag{A4}$$

where the subscript *fs* indicates the free-space Green's function (which will be used below), $k = \omega\sqrt{\mu\varepsilon}$ is wavenumber, and R is the distance between the observation point and the source point, and is given by

$$R = |\bar{r} - \bar{r}'| = \sqrt{(x - x')^2 + (y - y')^2 + (z - z')^2} . \tag{A5}$$

Thus, in free space the EFIE reduces to the following

$$\bar{E}^{i}_{\tan}(\bar{r}) = j\omega\mu \left\{ \left(1 + \frac{1}{k^2} \nabla\nabla \bullet \right) \oint_S \bar{J}_s(\bar{r}')\, G_{fs}(\bar{r}, \bar{r}')\ dS' \right\}_{\tan} . \tag{A6}$$

If the object is placed at the center of a parallel-plate waveguide with plate separation *d* (Figure A2) and we assume only the z-component is present, then the following three-dimensional Green's function must be used:

$$G(\bar{r}, \bar{r}') = G_{wg}(\bar{r}, \bar{r}') = \sum_{n=-\infty}^{\infty} \frac{e^{-jkR_n}}{4\pi R_n}, \tag{A7}$$

where

$$R_n = \sqrt{(x - x')^2 + (y - y' - nd)^2 + (z - z')^2} . \tag{A8}$$

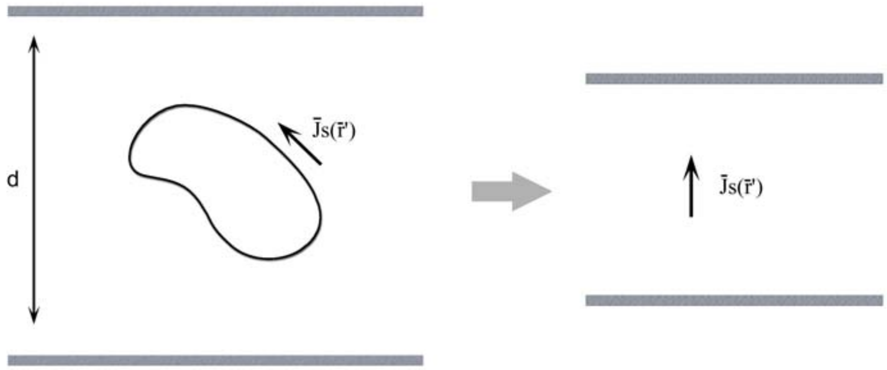

Figure A2: Metallic object placed in the center of a parallel-plate waveguide of separation *d*.

The Green's function can be re-expressed in terms of the free-space Green's function:

$$G(\bar{r},\bar{r}') = G_{wg}(\bar{r},\bar{r}') = G_{fs}(\bar{r},\bar{r}') + G_1(\bar{r},\bar{r}') + G_2(\bar{r},\bar{r}')\,, \tag{A9}$$

where

$$G_1(\bar{r},\bar{r}') = \sum_{n=1}^{\infty} \frac{e^{-jkR_n}}{4\pi R_n} \quad \text{and} \quad G_2(\bar{r},\bar{r}') = \sum_{n=-\infty}^{-1} \frac{e^{-jkR_n}}{4\pi R_n}\ . \tag{A10}$$

The Green's function $G_{wg}(\bar{r},\bar{r}')$ can be interpreted as a sum of the source and an infinite number of images lying along the *y*-axis (Figure A3).

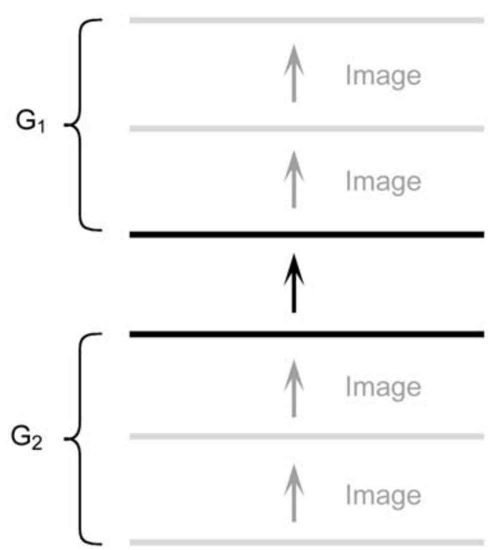

Figure A3: The metal walls create an infinite number of current images.

With the Green's function given in equation (A9), the EFIE reduces to the following for an object in a parallel-plate waveguide:

$$\begin{aligned}\bar{E}^{i}_{\tan}(\bar{r}) = j\omega\mu&\left\{\left(1+\frac{1}{k^2}\nabla\nabla\bullet\right)\oint_S \bar{J}_s(\bar{r}')\, G_{fs}(\bar{r},\bar{r}')\ dS'\right\}_{\tan} \\ &+ j\omega\mu\left\{\left(1+\frac{1}{k^2}\nabla\nabla\bullet\right)\oint_S \bar{J}_s(\bar{r}')\, G_1(\bar{r},\bar{r}')\ dS'\right\}_{\tan} \\ &+ j\omega\mu\left\{\left(1+\frac{1}{k^2}\nabla\nabla\bullet\right)\oint_S \bar{J}_s(\bar{r}')\, G_2(\bar{r},\bar{r}')\ dS'\right\}_{\tan}\end{aligned} \quad . \qquad \text{(A11)}$$

At this point, we can look at an approximate solution to the EFIE for the case when the object dimensions are small compared to the plate separation *d*. By assuming all dimensions of the object are small compared to the distance *d,* we make use of

$$\begin{aligned} x - x' &<< d \\ y - y' &<< d \\ z - z' &<< d \end{aligned} \quad , \qquad \text{(A12)}$$

and approximate R_n as

$$R_n \approx |nd| \quad \text{for} \quad \mathrm{n} \neq 0 . \qquad \text{(A13)}$$

Therefore, we have

$$G_1(\bar{r},\bar{r}') = \sum_{n=1}^{\infty} \frac{e^{-jk|nd|}}{4\pi\ |nd|} \quad \text{and} \quad G_2(\bar{r},\bar{r}') = \sum_{n=-\infty}^{-1} \frac{e^{-jk|nd|}}{4\pi |nd|} \ , \qquad \text{(A14)}$$

or

$$G_1(\bar{r},\bar{r}') \approx G_2(\bar{r},\bar{r}') \approx \sum_{n=1}^{\infty} \frac{e^{-jknd}}{4\pi\ nd} \quad . \qquad \text{(A15)}$$

The EFIE now reduces to

$$\begin{aligned}\bar{E}^{i}_{\tan}(\bar{r}) = j\omega\mu&\left\{\left(1+\frac{1}{k^2}\nabla\nabla\bullet\right)\oint_S \bar{J}_s(\bar{r}')\, G_{fs}(\bar{r},\bar{r}')\ dS'\right\}_{\tan} \\ &+ j2\omega\mu\left\{\left(1+\frac{1}{k^2}\nabla\nabla\bullet\right)\oint_S \bar{J}_s(\bar{r}')\sum_{n=1}^{\infty} \frac{e^{-jknd}}{4\pi\ nd}\ dS'\right\}_{\tan}\end{aligned} \quad . \qquad \text{(A16)}$$

All terms in the summation are independent of the integration variable, so that it can be brought outside the integral to give

$$\bar{E}^i_{\tan}(\bar{r}) = j\omega\mu \left\{ \left(1 + \frac{1}{k^2}\nabla\nabla \bullet \right) \oint_S \bar{J}_s(\bar{r}')\, G_{fs}(\bar{r},\bar{r}')\ dS' \right\}_{\tan} \quad . \tag{A17}$$
$$+ j2\omega\mu \sum_{n=1}^{\infty} \frac{e^{-jknd}}{4\pi\ nd} \left\{ \left(1 + \frac{1}{k^2}\nabla\nabla \bullet \right) \oint_S \bar{J}_s(\bar{r}')\ dS' \right\}_{\tan}$$

The summation is just a function of *kd*, and will be expressed as

$$S(kd) = \sum_{n=1}^{\infty} \frac{e^{-jknd}}{4\pi nd} \,. \tag{A18}$$

We will discuss of the summation in equation (A18) later. The integral in the second term on the right-hand side (RHS) of equation (A17) is just the total current on the object, a constant:

$$\bar{I} = \oint_S \bar{J}_s(\bar{r}')\ dS' , \tag{A19}$$

and the spatial derivatives in the second term on the RHS are zero. Therefore, the EFIE reduces to the following

$$\bar{E}^i_{\tan}(\bar{r}) = j\omega\mu \left\{ \left(1 + \frac{1}{k^2}\nabla\nabla \bullet \right) \oint_S \bar{J}_s(\bar{r}')\, G_{fs}(\bar{r},\bar{r}')\ dS' \right\}_{\tan} \quad . \tag{A20}$$
$$+ j2\omega\mu\ \bar{I}\ S(kd)$$

This expression can be rearranged to give

$$\bar{E}^i_{\tan}(\bar{r}) - \bar{C} = j\omega\mu \left\{ \left(1 + \frac{1}{k^2}\nabla\nabla \bullet \right) \oint_S \bar{J}_s(\bar{r}')\, G_{fs}(\bar{r},\bar{r}')\ dS' \right\}_{\tan} , \tag{A21}$$

where

$$\bar{C} = j2\omega\mu\ \bar{I}\ S(kd) \ . \tag{A22}$$

The EFIE given in equation (A21) is similar to the EFIE given in equation (A6). The RHS is the same and the left-hand-side (LHS) has been modified by $\bar{C}$. This term can be considered a correlation term. The parallel-plate waveguide has the effect of modifying the incident field on the object when the object dimensions are small compared to *d*.

Now take a close look at $S(kd)$. Certain values of kd will cause the summation to become infinite. In particular, for $kd = 2m\pi$ we have

$$S(kd) = \sum_{n=1}^{\infty} \frac{e^{-jn(2m\pi)}}{4\pi n d}. \tag{A23}$$

The exponential can be expressed in terms of trigonometric functions to give

$$\sum_{n=1}^{\infty} \frac{e^{-jn(2m\pi)}}{4\pi nd} = \frac{1}{4\pi d} \sum_{n=1}^{\infty} \left(\frac{\cos(n(2m\pi))}{n} - j\frac{\sin(n(2m\pi))}{n} \right) . \tag{A24}$$

For any integer value of *m* we have:

$$\cos(n(2m\pi\,)) = 1 \quad \text{and} \quad \sin(n(2m\pi\,)) = 0 \ , \tag{A25}$$

which gives

$$\sum_{n=1}^{\infty} \frac{e^{-jn(2m\pi)}}{4\pi nd} = \frac{1}{4\pi d} \sum_{n=1}^{\infty} \frac{1}{n} = \infty\ . \tag{A26}$$

Therefore, we see that for

$$kd = 2m\pi \quad \text{or} \quad d = m\lambda \quad , \tag{A27}$$

a resonant condition occurs that is equivalent to all the image terms adding constructively. For $d = m\lambda$, the correction term $\overline{C}$ become infinite and, as a result, the currents on the object obtained from the EFIE in equation (A21) will be very different from the current on the same object in free-space (see equation (A6)).

This result follows from evaluating the summation, which is done by expressing the exponential in terms of trigonometric functions:

$$\sum_{n=1}^{\infty} \frac{e^{-jknd}}{4\pi nd} = \frac{1}{4\pi d} \sum_{n=1}^{\infty} \left(\frac{\cos(nkd)}{n} - j\frac{\sin(nkd)}{n} \right) . \tag{A28}$$

Each term of this infinite sum can be evaluated for $0 \le kd \le 2\pi$ to give [6]

$$\sum_{n=1}^{\infty} \frac{\cos(nkd)}{n} = -\frac{1}{2} ln\left[2(1-\cos(kd))\right] \ \text{for} \ 0 \le kd \le 2\pi\ , \tag{A29}$$

and

$$\sum_{n=1}^{\infty} \frac{\sin(nkd)}{n} = \frac{\pi - kd}{2} \quad \text{for} \quad 0 \le kd \le 2\pi \, , \tag{A30}$$

and

$$\sum_{n=1}^{\infty} \frac{e^{-jknd}}{4\pi nd} = -\frac{1}{8\pi d} \quad \left\{ ln\left[2(1 - cos(kd))\right] + j\left(\pi - kd\right) \right\} \quad \text{for} \quad 0 \le kd \le 2\pi \, . \tag{A31}$$

While the summation is stated as being valid for $0 \le kd \le 2\pi$, recognize that the function in the summation has period 2π. Therefore the expression in equation (A31) is valid for all kd as long as one correctly repeats the value of the function (kd) every 2π (i.e., every 2π set $kd = 0$).

From equation (A31) it is observed that the logarithm term is the dominant term at ($kd = 2m\pi$), where it is singular. Figure A4 shows a plot of this logarithm term as a function of kd (or d / λ). The figure clearly illustrates the resonant behavior of the parallel-plate waveguide when

$$d = m\lambda \, . \tag{A32}$$

With the evaluation of the summation in equation (A31), the correction term $\overline{C}$ reduces to

$$\overline{C} = -j \frac{\omega\mu}{4\pi d} \quad \overline{I} \left\{ ln\left[2(1 - \cos(kd))\right] + j\left(\pi - kd\right) \right\} \, . \tag{A33}$$

Therefore, the current on the object will be only slightly modified from the currents on the same object in free-space except at resonances which occurs when

$$d = m\lambda \, . \tag{A34}$$

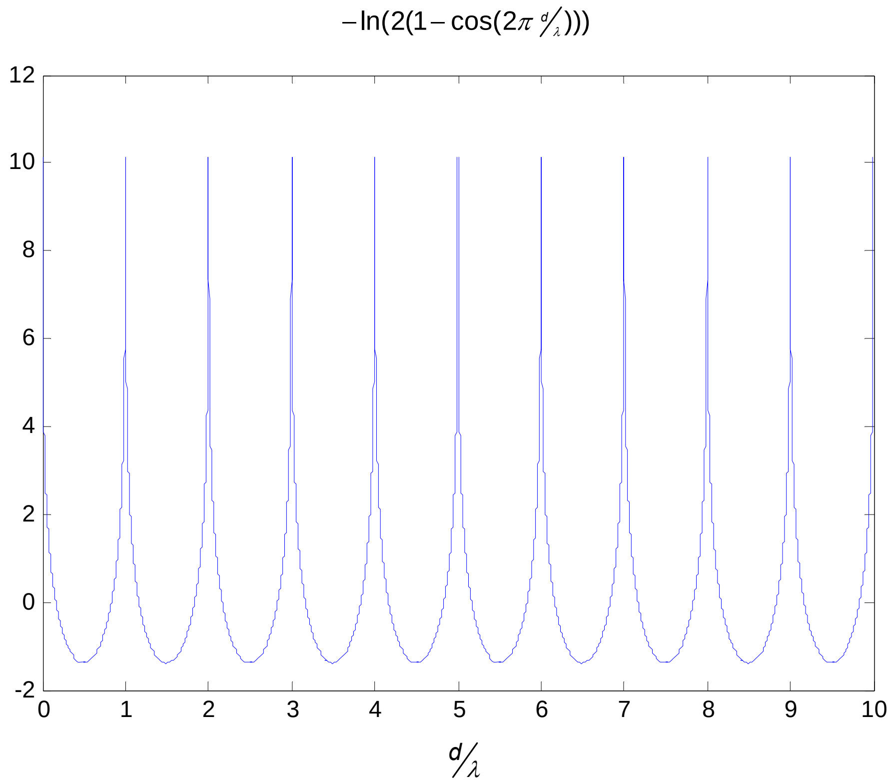

Figure A4: Functional form of the logarithm term in equation (A33) with respect to kd (or d/λ).

Appendix References

[1] Lindell, I.V. Methods for Electromagnetic Fields Analysis. Chapter 6; Piscataway, N.J.: IEEE Press; 1992.

[2] Wang, J. H. Generalized Moment Methods in Electromagnetics. Chapter 3; New York: John Wiley & Sons, Inc.; 1991.

[3] Morita, N.; Kumagai, N.; Mautz, J. R., Integral Equation Methods for Electromagnetics. Boston: Artech House; 1990.

[4] Balanis, C. A. Advanced Engineering Electromagnetics. Chapter 12; N.Y.: John Wiley & Sons, Inc.; 1989.

[5] Noble, B. Integral equation perturbation methods in low-frequency diffraction in Electromagnetic Waves. pp. 323-360; R.E. Langer, editor. Madison: The University of Wisconsin Press; 1962.

[6] Wheelon, A. D. Tables of Summable Series and Integral Involving Bessel Functions. San Francisco: Holden-Day, 1968.

NIST ***Technical Publications***

Periodical

Journal of Research of the National Institute of Standards and TechnologyCReports NIST research and development in metrology and related fields of physical science, engineering, applied mathematics, statistics, biotechnology, and information technology. Papers cover a broad range of subjects, with major emphasis on measurement methodology and the basic technology underlying standardization. Also included from time to time are survey articles on topics closely related to the Institute's technical and scientific programs. Issued six times a year.

Nonperiodicals

MonographsCMajor contributions to the technical literature on various subjects related to the Institute's scientific and technical activities.
HandbooksCRecommended codes of engineering and industrial practice (including safety codes) developed in cooperation with interested industries, professional organizations, and regulatory bodies.
Special PublicationsCInclude proceedings of conferences sponsored by NIST, NIST annual reports, and other special publications appropriate to this grouping such as wall charts, pocket cards, and bibliographies.
National Standard Reference Data SeriesCProvides quantitative data on the physical and chemical properties of materials, compiled from the world's literature and critically evaluated. Developed under a worldwide program coordinated by NIST under the authority of the National Standard Data Act (Public Law 90-396). NOTE: The Journal of Physical and Chemical Reference Data (JPCRD) is published bimonthly for NIST by the American Institute of Physics (AIP). Subscription orders and renewals are available from AIP, P.O. Box 503284, St. Louis, MO 63150-3284.
Building Science SeriesCDisseminates technical information developed at the Institute on building materials, components, systems, and whole structures. The series presents research results, test methods, and performance criteria related to the structural and environmental functions and the durability and safety characteristics of building elements and systems.
Technical NotesCStudies or reports which are complete in themselves but restrictive in their treatment of a subject. Analogous to monographs but not so comprehensive in scope or definitive in treatment of the subject area. Often serve as a vehicle for final reports of work performed at NIST under the sponsorship of other government agencies.
Voluntary Product StandardsCDeveloped under procedures published by the Department of Commerce in Part 10, Title 15, of the Code of Federal Regulations. The standards establish nationally recognized requirements for products, and provide all concerned interests with a basis for common understanding of the characteristics of the products. NIST administers this program in support of the efforts of private-sector standardizing organizations.

Order the ***following*** *NIST publications*C*FIPS and NISTIRs*C*from the National Technical Information Service, Springfield, VA 22161.*

Federal Information Processing Standards Publications (FIPS PUB)CPublications in this series collectively constitute the Federal Information Processing Standards Register. The Register serves as the official source of information in the Federal Government regarding standards issued by NIST pursuant to the Federal Property and Administrative Services Act of 1949 as amended, Public Law 89-306 (79 Stat. 1127), and as implemented by Executive Order 11717 (38 FR 12315, dated May 11,1973) and Part 6 of Title 15 CFR (Code of Federal Regulations).
NIST Interagency or Internal Reports (NISTIR)CThe series includes interim or final reports on work performed by NIST for outside sponsors (both government and nongovernment). In general, initial distribution is handled by the sponsor; public distribution is handled by sales through the National Technical Information Service, Springfield, VA 22161, in hard copy, electronic media, or microfiche form. NISTIRs may also report results of NIST projects of transitory or limited interest, including those that will be published subsequently in more comprehensive form.

U.S. Department of Commerce
National Bureau of Standards and Technology
325 Broadway
Boulder, CO 80305-3328